

Three-dimensional deep learning-based reduced order model for unsteady flow dynamics with variable Reynolds number

Rachit Gupta^{a)} and Rajeev Jaiman^{b)}

Department of Mechanical Engineering, University of British Columbia, V6T 1Z4, Canada

(Dated: 20 December 2021)

In this article, we present a deep learning-based reduced order model (DL-ROM) for predicting the fluid forces and unsteady vortex shedding patterns. We consider the flow past a sphere to examine the accuracy of our DL-ROM predictions. The proposed DL-ROM methodology relies on a three-dimensional convolutional recurrent autoencoder network (3D CRAN) to extract the low-dimensional flow features from the full-order snapshots in an unsupervised manner. The low-dimensional features are evolved in time using a long short-term memory-based recurrent neural network (LSTM-RNN) and reconstructed back to the full-order as flow voxels. These flow voxels are introduced as static and uniform query probes in the point cloud domain to reduce the unstructured mesh complexity while providing convenience in the 3D CRAN training. We analyze a novel procedure to recover the interface description and the instantaneous force quantities from these 3D flow voxels. The 3D CRAN-based DL-ROM methodology is first applied to an external flow past a static sphere at single Reynolds number (Re) of $Re = 300$ to test the 3D flow reconstruction and inference. We provide an assessment of the computing requirements in terms of the memory usage, training costs and testing times associated with the 3D CRAN framework. Subsequently, variable Re -based flow information is infused in one 3D CRAN to learn a complicated symmetry-breaking flow regime ($280 \leq Re \leq 460$) for the flow past a sphere. Effects of transfer learning are analyzed for training this complicated 3D flow regime on a relatively smaller time series dataset. The 3D CRAN framework learns the complicated flow regime nearly 20 times faster than the parallel full-order model and predicts this flow regime in time with an excellent to good accuracy. Based on the predicted flow fields, the network demonstrates an R^2 accuracy of 98.58% for the drag and 76.43% for the lift over the sphere in this flow regime. The proposed framework aligns with the development of a digital twin for 3D unsteady flow field and instantaneous force predictions with variable Re effects.

Keywords: 3D unsteady flows; Force prediction; Deep learning-based reduced-order model; Recurrent and convolutional neural networks; Autoencoders; Digital twin;

I. INTRODUCTION

Unsteady flows described by the Navier-Stokes partial differential equation (PDE) possess highly nonlinear and multi-scale characteristics. In particular, the underlying flow phenomenon due to the features (e.g., flow separation, shear layer, vortex shedding, near wake) exhibits complex spatial-temporal dynamics as functions of geometry and physical parameters³⁹. Examples of such spatial-temporal behaviors include the flow past fluttering flags and thin foils²⁰, oscillating hydrofoils with cavitation³², two-phase flows with fluid-structure interaction in offshore and marine applications³⁰ and among others. An accurate understanding of the unsteady flow features and their physical interactions is essential for operational decisions, structural designs, and the development of control strategies. The predictions of the unsteady flows are widely investigated and accurately modeled via reliable numerical methods based on PDEs that describe physical laws. Using state-of-the-art discretizations such as the finite element method, accurate solutions have been possible by solving millions of flow variables using full-order methods on high-dimensional PDEs. These techniques primarily involve solving the unsteady Navier-Stokes equations in a 3D computational domain for various geometries and boundary condi-

tions which can involve moving interfaces and fluid-structure interaction²⁷.

While the full-order modeling techniques provide high fidelity data, it is well known that such techniques are computationally expensive. Furthermore, the analysis of flow involving three-dimensional geometries involves high resolutions near the interface. This results in the generation of a large number of unknown variables for accuracy gains and thereby scales the model's fidelity to millions of variables. Running such high-resolution and multi-scale simulations with regular PDE discretization requires a large computational time even in the supercomputing environment. As a result, the forward and high-dimensional problems become less attractive for multi-query analysis, control and structural design optimization.

A. Deep learning-based reduced order modeling

For addressing issues of high-dimensionality, reduced-order models (ROMs) are instead constructed for low-dimensional analysis and have been widely investigated to identify dominant flow patterns and make dynamical predictions. One of the principal tools is to project a high-dimensional dataset onto an optimal low-dimensional subspace either linearly or nonlinearly to reduce spatial dimension and extract flow features. These low-dimensional analyses can provide essential flow dynamics for operational decision and efficiency improvement. Various projection tech-

^{a)}Electronic mail: rachit.gupta@ubc.ca

^{b)}Electronic mail: rjaiman@mech.ubc.ca

niques such as proper orthogonal decomposition (POD)⁵⁴, dynamic mode decomposition (DMD)⁵², balanced-POD⁵³ and Koopman operators⁴⁵ have been extensively studied for the dimensionality reduction, control and mode decomposition of field dataset into relevant features. The mode decomposition can be considered as a mathematically optimal linear representation of the flow field and can provide interpretable analysis on flow features. For instance, Miyanawala and Jaiman³⁹ showcased that for flows involving low Re , the POD modes represent one of the large-scale flow features such as vortex shedding, shear layer or near-wake bubble.

However, projection-based ROMs can pose difficulty in the dimensionality reduction for complex flow patterns and hyperbolic PDEs as the number of required modes increases significantly. Instead, neural network-based autoencoders^{3,47} are explored as an alternative for nonlinear approximation because of their ability to automatically encode flow datasets and address some of the limitations of linear projection techniques. Using encoder-decoder networks and activation functions, autoencoders allow to learn nonlinear relations between the input and the output dataset. In contrast to the projection-based ROMs, autoencoders provide larger compression and a greater flexibility for the dimensionality reduction of the data arising from the Navier-Stokes equations. Autoencoders have been employed in a variety of fields such as object detection⁴⁴, sensor data-analysis³⁷ and biometric recognition⁵⁷ due to their ease of implementation and low computational cost. For autoencoder and its variants, one can refer to a review work of Dong *et al.*¹⁴. To achieve data-driven prediction of dynamical problems using projecting methods, many researchers combine ROM spaces with deep learning to enhance predictive abilities which can be termed hybrid DL-ROMs. Such hybrid architectures consider spatio-temporal domain knowledge and achieve data-driven time series predictions. Recently proposed POD-based DL-ROMs are the POD-CNN by Miyanawala and Jaiman⁴⁰, the POD-RNN by Bukka *et al.*⁷, the POD-enhanced autoencoders by Fresca and Manzoni¹⁷. These hybrid architectures have been demonstrated for 2D bluff body flows with and without fluid-structure interaction.

B. Review of physics-based deep learning

Deep learning in physical simulation has been boosting from the past decade owing to its effectiveness to automatically classify functional relations and make inference from a set of training data. Deep neural networks rely on the universal approximation of functions^{12,13,23}. Despite the fact that deep neural networks are heavily overparametrized, they have an inherent bias to induce and make inferences from unseen data, which is known as inductive bias⁵. Convolutional neural nets, for example, have an implicit inductive bias due to shared weight convolutional filters (i.e., translational symmetry) and pooling to exploit scale separation⁵. However, these black-box deep learning techniques ignore prior domain knowledge, which is crucial for interpretability, data efficiency, and generalization.

Many promising approaches have been established in the

research community for a synergistic coupling of deep learning and physics-based models^{7,9}. These models are trained to represent a full or partial parametrization of a forward process to reduce computational costs while emulating physical laws. For instance, the trained parameters can be used to achieve the state-to-state time advancements^{6,21,50} and inverse modeling^{11,36,43}. The state-to-state time advancement implies inferring dependent physical variables from the previous states. Inverse modeling, on the other hand, identifies physical system parameters from output state data. In order to increase generality, we can divide the physics-based machine learning into three categories: (a) adding a regularizer to the objective or loss function, (b) modifying neural architecture designs, and (c) combining deep learning and projection-based model reduction.

In the first category, physical losses are applied to the objective functions using regularizers in neural networks. These networks are trained to solve supervised learning tasks while adhering to governing equations. For instance Karpatne *et al.*³¹, Raissi *et al.*⁴⁹, Zhu *et al.*⁵⁸, Erichson *et al.*¹⁶ and among others have applied such regularizers to boost generalizability while training neural networks. Wang *et al.*⁵⁶ also employed physics-informed machine learning to model the reconstruction of inconsistencies in the Reynolds stresses. As the second category of neural architectural designs, convolutional neural networks are utilized for the prediction of steady laminar flows¹⁸ and the bulk quantities of interest³⁸ for bluff bodies. Similarly, Lee *et al.*³⁴ employed CNNs and generative adversarial networks (GANs) with and without loss function modification to predict recursive unsteady flows. For the prediction of unsteady flow over a cylinder and airfoil, Han *et al.*²² constructed a convolutional long-short term memory (LSTM) network. To estimate the drag force, Ogoke *et al.*⁴² developed a graph-based convolutional neural network by depicting the flow field around an airfoil using unstructured grids. Likewise, Snachez *et al.*⁵¹ and Pfaff *et al.*⁴⁶ utilized graph neural networks to represent the state of a physical system as nodes in a graph and compute the dynamics by learning message-passing signals. The third category in the physics-based deep learning involves the development of the hybrid DL-ROMs that take into account the spatial and temporal domain knowledge in neural networks^{7,17,19,40}. We refer to such DL-ROM frameworks as physics-based because they incorporate physical interpretability via proper orthogonal decomposition and its variants.

C. Gaps and our contribution

Using physics-based deep learning, the above works report substantial speed-ups during the online predictions compared with their full-order counterpart. However, most of these works are centered around two-dimensional geometries^{4,15,18,28,41}. In this paper, we develop a deep learning-based reduced-order modeling framework for (a) three-dimensional unsteady flow predictions, (b) parametric flow and force predictions with variable Reynolds number, and (c) data-driven computational speed-ups for both offline

training and online prediction of complex 3D wake flow. Although there are a few studies that use CNNs and autoencoder for parametric dependent flow problems^{17,34}, there is no work that attempts to develop a DL-ROM methodology for the flow past 3D geometries in a way that can provide an effective mean to couple with real-time flow field snapshots^{35,48}.

The present work builds upon our previous works^{7,19} on the development of a convolutional recurrent autoencoder framework for three-dimensional flow past a sphere. Specifically, the present work utilizes 3D CNNs to extract low-dimensional features from full-order flow snapshots. The LSTM-RNN is utilized to evolve the low-dimensional features in time. Through 3D convolutional architecture, we model the flow variables in a uniform voxel grid. Using an unstructured irregular grid for the full-order simulation, we utilize snapshot-field transfer and load recovery (snapshot-FTLR)¹⁹ to select the structured grid for the fluid domain via interface force recovery. This simplified procedure reduces the unstructured mesh complexity while providing convenience in the training of the 3D CRAN framework. We emphasize the learning and inference capabilities of 3D CRAN on a complicated variable Re flow regime for flow past a sphere. Using transfer learning, we reduce the offline training time and hyperparameter search of 3D CRAN. With the transfer learning process, this 3D CRAN maintains speed-up in training and provides a coarse-grained learning model for 3D unsteady flows compared with the FOM. The proposed DL-ROM provides a near real-time prediction of 3D flow fields and forces with variable Reynolds numbers. The end-to-end DL-ROM framework is 3D and entirely data-driven; hence, it aligns with developing a digital twin involving variable Re information.

The article is organized as follows: Section II describes the full-order governing equations and reduced-order modeling of flow fields. Section III introduces the voxel-based data generation process from full-order flow fields. Section IV presents the DL-ROM methodology employing 3D CNNs, convolutional recurrent autoencoder network, and transfer learning. The implementation of the proposed DL-ROM for the flow past a sphere with single and variable Re is demonstrated in section V. The article ends with the discussion on the variation of predicted forces to Re and concluding remarks in section VI.

II. FULL-ORDER AND REDUCED-ORDER MODELING

This section starts by describing the full-order governing equations of the incompressible Navier-Stokes, followed by a brief description of reduced-order modeling.

A. Full-order modeling

The isothermal viscous fluid in an Eulerian domain $\Omega^f(t)$ can be described using the incompressible Navier-Stokes

equations as:

$$\rho^f \frac{\partial \mathbf{u}^f}{\partial t} + \rho^f \mathbf{u}^f \cdot \nabla \mathbf{u}^f = \nabla \cdot \boldsymbol{\sigma}^f + \mathbf{b}^f \quad \text{on } \Omega^f(t), \quad (1)$$

$$\frac{\partial \rho^f}{\partial t} + \nabla \cdot (\rho^f \mathbf{u}^f) = 0 \quad \text{on } \Omega^f(t), \quad (2)$$

where the fluid variables are denoted using the superscripts f . Here, \mathbf{u}^f , \mathbf{b}^f and $\boldsymbol{\sigma}^f$ represent the fluid velocity, body force and Cauchy stress tensor, respectively. For a Newtonian fluid with density ρ^f and dynamic viscosity μ^f , $\boldsymbol{\sigma}^f = -p^f \mathbf{I} + \mu^f (\nabla \mathbf{u}^f + (\nabla \mathbf{u}^f)^T)$. Here, \mathbf{I} represents the identity tensor and p^f denotes the hydrodynamic pressure in the fluid. The partial time derivatives in Eqs. (1)-(2) is with respect to the Eulerian referential coordinate system \mathbf{x}^f and must satisfy the boundary conditions in the fluid domain

$$\mathbf{u}^f = \mathbf{u}_D^f \quad \forall \quad \mathbf{x}^f \in \Gamma_D^f, \quad (3)$$

$$\boldsymbol{\sigma}^f \cdot \mathbf{n}^f = \mathbf{h}^f \quad \forall \quad \mathbf{x}^f \in \Gamma_N^f, \quad (4)$$

$$\mathbf{u}^f = \mathbf{u}_0^f \quad \text{on } \Omega^f(0). \quad (5)$$

While \mathbf{u}_0^f is the initial condition, \mathbf{u}_D^f and \mathbf{h}^f represent the Dirichlet and Neumann boundary conditions on Γ_D^f and Γ_N^f , respectively. \mathbf{n}^f denotes the unit normal on Γ_N^f . The fluid-solid interface Γ^{fs} in the fluid domain is modeled using a no-slip Dirichlet boundary condition via Eq. (3) with $\mathbf{u}_D^f = 0$. The fluid force along the fluid-solid boundary is computed by integrating the surface traction, from the Cauchy stress tensor, over the first boundary layer elements on the fluid-solid surface. At a time instant, the force coefficients C_x , C_y and C_z in the respective Cartesian directions are given as

$$\begin{aligned} C_x &= \frac{1}{\frac{1}{2} \rho^f U_\infty^2 D} \int_{\Gamma^{fs}} (\boldsymbol{\sigma}^f \cdot \mathbf{n}) \cdot \mathbf{n}_x d\Gamma, \\ C_y &= \frac{1}{\frac{1}{2} \rho^f U_\infty^2 D} \int_{\Gamma^{fs}} (\boldsymbol{\sigma}^f \cdot \mathbf{n}) \cdot \mathbf{n}_y d\Gamma, \\ C_z &= \frac{1}{\frac{1}{2} \rho^f U_\infty^2 D} \int_{\Gamma^{fs}} (\boldsymbol{\sigma}^f \cdot \mathbf{n}) \cdot \mathbf{n}_z d\Gamma, \end{aligned} \quad (6)$$

where U_∞ and D are the reference velocity and reference length, respectively. For the unit normal \mathbf{n} of the surface, \mathbf{n}_x , \mathbf{n}_y and \mathbf{n}_z are the x, y and z Cartesian components, respectively. The weak form of the incompressible Navier-Stokes equations is solved in space using an equal-order isoparametric finite elements for the fluid velocity and pressure. A numerical scheme implementing the Petrov-Galerkin finite element and the semi-discrete time stepping is utilized^{25,26} to generate the full-order 3D flow states.

B. Reduced-order modeling

In relation to the reduced-order modeling of these state variables, the PDEs described by Eqs. (1)-(2) can be re-written in an abstract state-space form as

$$\frac{d\mathbf{y}}{dt} = \mathbf{F}(\mathbf{y}), \quad (7)$$

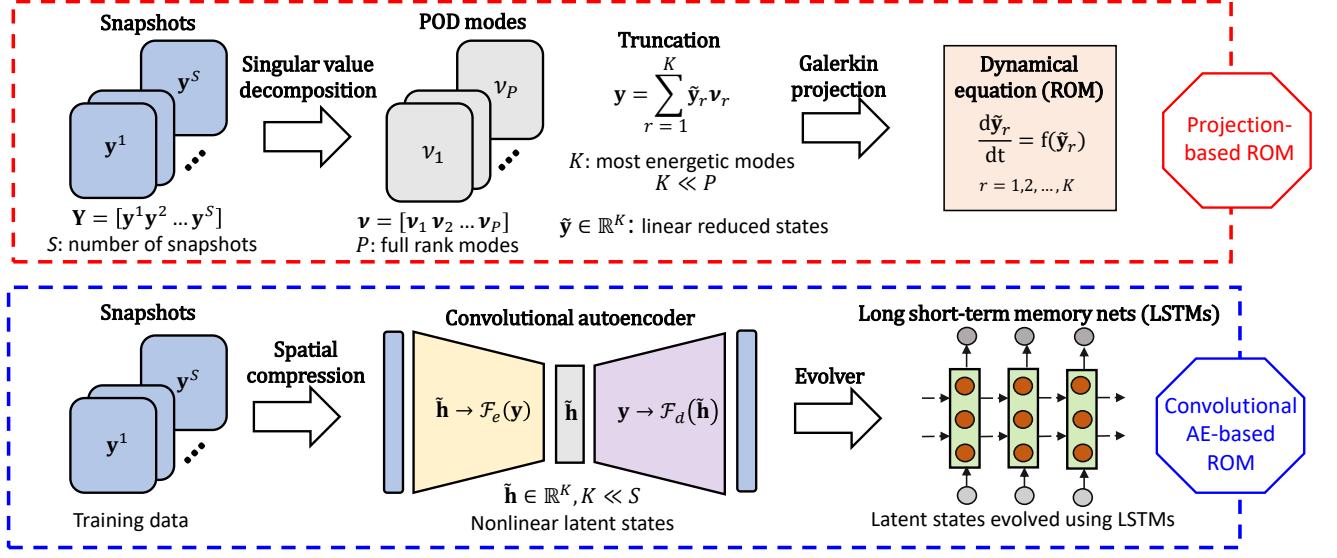


FIG. 1: Illustration of reduced-order modeling: (i) Projection-based ROM for creating orthonormal basis functions (modes) for the reduced representation and (ii) convolutional autoencoder ROM framework. Refer to the details of the variables in the main text in section II B.

$\mathbf{y} \in \mathbb{R}^M$ represents a state vector consisting of M system variables, while $d\mathbf{y}/dt$ is the dynamics of the state vector. In the present case, the state vector consists of the fluid velocity and the pressure dataset as $\mathbf{y} = \{\mathbf{u}^f, p^f\}$. \mathbf{F} denotes a vector-valued differential operator describing the spatially discretized PDEs. The spatial-temporal dynamical equation is useful for creating the reduced-order approximation of a coupled dataset. In reduced-order modeling, the differential operator \mathbf{F} is constructed by projecting the full-order state variables on a trial subspace. For this purpose, $\mathbf{F}(\mathbf{y})$ is decomposed into the constant \mathbf{C} , linear $\mathbf{B}\mathbf{y}$ and nonlinear $\mathbf{F}'(\mathbf{y})$ dynamical components as

$$\mathbf{F}(\mathbf{y}) = \mathbf{C} + \mathbf{B}\mathbf{y} + \mathbf{F}'(\mathbf{y}). \quad (8)$$

1. Projection-based reduced order modeling

The Galerkin-based ROMs project the state vector $\mathbf{y} \in \mathbb{R}^M$ via a subspace spanned $\mathcal{V} \in \mathbb{R}^{M \times K}$. The subspace matrix \mathcal{V} represents the reduced basis onto which the full-order dynamics is generally projected with $K \ll M$. This reduces the full-order state vector \mathbf{y} as $\mathcal{V}\tilde{\mathbf{y}}$ with $\tilde{\mathbf{y}} \in \mathbb{R}^K$ and thereby approximating the system dynamics using Eqs. (7)-(8) as

$$\frac{d\tilde{\mathbf{y}}}{dt} = \mathcal{V}^T \mathbf{C} + \mathcal{V}^T \mathbf{B} \mathcal{V} \tilde{\mathbf{y}} + \mathcal{V}^T \mathbf{F}'(\mathcal{V} \tilde{\mathbf{y}}). \quad (9)$$

The reduced-order space is defined by a set of modes $\mathcal{V} \in \mathbb{R}^{M \times K}$ using the snapshot matrix $\mathbf{Y} = \{\mathbf{y}^1 \mathbf{y}^2 \dots \mathbf{y}^S\} \in \mathbb{R}^{M \times S}$, with M number of variables and S denotes the number of snapshots. The projection forms an orthonormal basis of $\tilde{\mathbf{Y}} = \{\tilde{\mathbf{y}}^1 \tilde{\mathbf{y}}^2 \dots \tilde{\mathbf{y}}^S\} \in \mathbb{R}^{K \times S}$, a K dimensional subspace of \mathbb{R}^M . For example, the POD method first creates the orthonormal

basis functions for the reduced representation, which is followed by the Galerkin projection onto the subspace spanned by a set of truncated basis functions⁵⁵. While these projection-based models are effective in constructing a low-dimensional subspace of low Kolmogorov n -width problems, they may not provide efficient reconstruction for general nonlinear systems. As a further approximation of these nonlinear systems for efficiency, hyperreduction techniques such as the discrete empirical interpolation method¹⁰ and energy-conserving sampling and weighting² method can be employed. However, these empirical projection-based reduced-order models can come at the cost of large subspace dimensions for convection-dominated or turbulence problems characterized by large Kolmogorov n -width.

2. Autoencoder-based reduced order modeling

The drawbacks of the projection-based ROMs can be addressed by the use of autoencoders that provide a promising alternative for constructing the reduced-order space of the snapshot matrix \mathbf{Y} . An autoencoder comprises an encoder and decoder network and can be interpreted as a nonlinear and flexible generalization of POD for a dimensionality reduction of flow field⁸. An autoencoder, \mathcal{F} , is trained to output the same input data \mathbf{Y} so that $\mathbf{Y} \approx \mathcal{F}(\mathbf{Y}; w)$, where w are the parameters of the end-to-end autoencoder model. Using an iterative minimization of an error function E , the parameters w are trained as

$$w = \operatorname{argmin}_w [E(\mathbf{Y}, \mathcal{F}(\mathbf{Y}; w))]. \quad (10)$$

The dimension of the low-order space $\tilde{\mathbf{H}}$ in an autoencoder is smaller than that of the input or output data \mathbf{Y} and is re-

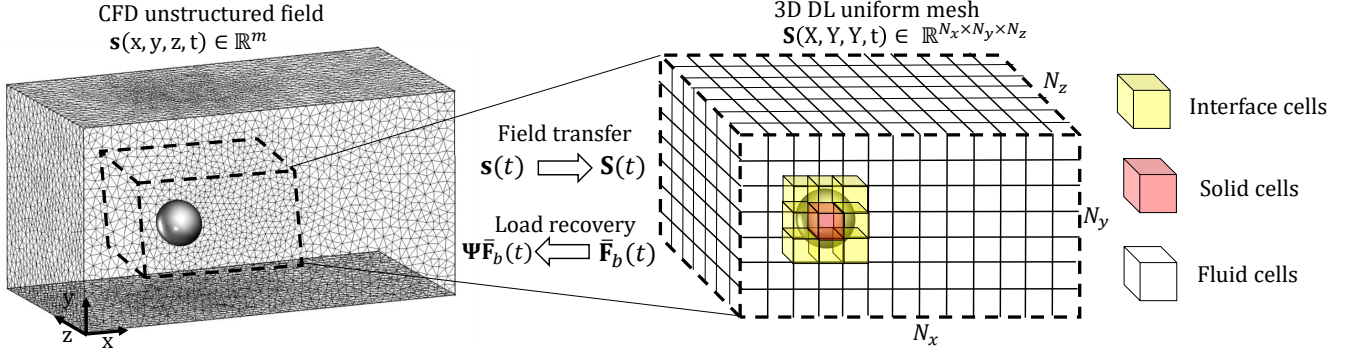


FIG. 2: Schematic of a 3D mesh-to-mesh field transfer and load recovery process to determine the 3D CRAN snapshot grid. Refer to the details of all variables in section III.

ferred to as a latent space. When the output $\mathcal{F}(\mathbf{Y})$ is comparable to the input such that $\mathbf{Y} \approx \mathcal{F}(\mathbf{Y})$, the latent space is a low-dimensional representation of its input which provides a low-rank embedding. The dimension compressor in an autoencoder is called the encoder \mathcal{F}_e , and the counterpart is the decoder \mathcal{F}_d . The internal mechanism of the autoencoder can be stated as follows using the encoder-decoder architecture:

$$\tilde{\mathbf{H}} = \mathcal{F}_e(\mathbf{Y}), \quad \mathbf{Y} = \mathcal{F}_d(\tilde{\mathbf{H}}). \quad (11)$$

The subspace projection in an autoencoder is achieved using an unsupervised training of the snapshot matrix \mathbf{Y} . Throughout the paper, we utilize the convolutional autoencoder process for general reduced-order modeling. In particular, a 3D convolutional mapping in the autoencoder can provide an efficient latent space to characterize the reduced dynamics of 3D unsteady flows. After convergence, linear autoencoders with a latent dimension of K span the same subspace as POD using K modes as illustrated in^{3,47}. In the next section, we turn our attention toward an optimal procedure for selecting the full-order dataset for a 3D convolutional autoencoder.

III. FIELD TRANSFER AND COARSE GRAINING

Flow simulations involving bluff body flows are generally modeled in a non-uniform and unstructured body conformal mesh for computational fluid dynamics (CFD) applications. Primarily, an unstructured mesh offers the advantage of allocating a greater node resolution in the region of importance in the flow domain, for example, the boundary layer mesh along the fluid-solid interface. Although creating an unstructured mesh for CFD problems can provide an accurate interface modeling, the number of nodes can scale to millions of variables for the fluid domain. This generally results in a point cloud domain with complex spatial connectivity information for every bluff body geometry. The complex mesh connectivity information can be directly difficult to incorporate in a neural network especially involving the use of CNN filters. As a result, the time series flow snapshots are point cloud information that may not contain spatial connectivity information in the dataset.

To retain the spatial connectivity information in the dataset, we project the unstructured field dataset on a uniform and structured voxel grid to coarse-grain the field information as shown in Fig. 2. This simple process brings uniformity in the field information together with convenience in training the CRAN driver. The projection and interpolation of information are achieved via the snapshot-field transfer and load recovery process introduced in the following subsections. Snapshot-FTLR is an iterative data processing step that allows recoverable interface information by preserving the forces. Once this loss is observed in the training forces, they are corrected by reconstructing to a higher-order CFD force.

A. Field transfer

We extend the snapshot-FTLR to 3D flow fields throughout this paper. Let $\mathbf{s} = \{\mathbf{s}^1 \mathbf{s}^2 \dots \mathbf{s}^n\} \in \mathbb{R}^{m \times n}$ be the full-order flow fields generated from the Navier-Stokes solver and $\bar{\mathbf{F}}_{\Gamma_{fs}} = \{\bar{\mathbf{F}}_{\Gamma_{fs}}^1 \bar{\mathbf{F}}_{\Gamma_{fs}}^2 \dots \bar{\mathbf{F}}_{\Gamma_{fs}}^n\} \in \mathbb{R}^{3 \times n}$ be the corresponding interface forces over the fluid-solid body along the three Cartesian directions. Here, m represent the number of full-order nodes and n denotes the number of snapshots. The point cloud dataset at every time step is interpolated and projected to a uniform voxel grid as shown in Fig. 2. The size of this grid can be chosen $(N_x \times N_y \times N_z)$. N_x , N_y and N_z are the data probes in the respective Cartesian axes. These probes are structured as spatially uniform 3D space for coarse-graining the field information as well as retaining a uniform mesh connectivity. We employ Scipy's *griddata* function¹ to interpolate the scattered CFD data and fit a surface to generate the 3D flow snapshots. The generated information $\mathbf{S} = \{\mathbf{S}^1 \mathbf{S}^2 \dots \mathbf{S}^n\} \in \mathbb{R}^{N_x \times N_y \times N_z \times n}$ denotes the 3D snapshots of a field dataset (for instance, pressure or velocity), where $\mathbf{S}^i \in \mathbb{R}^{N_x \times N_y \times N_z}$.

B. Load recovery

The presence of the interface in the DL voxel grid is ensured by masking the entire 3D spatial region covered by the solid domain with a mandatory function which zeroes out the field

values inside the fluid-solid interface. This function identifies the coarse interface voxels (shown as yellow cells in Fig. 2) that contain the solid description. We now integrate the total voxel force $\bar{\mathbf{F}}_b = \{\bar{\mathbf{F}}_b^1 \bar{\mathbf{F}}_b^2 \dots \bar{\mathbf{F}}_b^n\}$ exerted by these interface cells over the solid using

$$\bar{\mathbf{F}}_b^i = \sum_{k=1}^{N_F} \int_{\Gamma^k} \boldsymbol{\sigma}_k^i \cdot \mathbf{n} d\Gamma, \quad i = 1, 2, \dots, n, \quad (12)$$

where N_F are the number of interface voxels. For every interface cell k , $\boldsymbol{\sigma}_k^i$ is the Cauchy stress tensor at a time step t^i . We calculate this tensor using the finite difference approximation and integrate over the faces of the voxel Γ^k . For the present case, we only consider the pressure component while calculating the voxel forces.

The coarsening effect of the full-order data onto the voxel grid brings a spatial uniformity in the input state. However, this coarsening may also lead to a loss of accurate forces on the physical interface, even in the training data. This is accounted due to a considerable loss of interface resolution in the voxel grid as compared with the FOM mesh. Herein, we recover the data loss in the voxel forces $\bar{\mathbf{F}}_b = \{\bar{\mathbf{F}}_b^1 \bar{\mathbf{F}}_b^2 \dots \bar{\mathbf{F}}_b^n\}$ by mapping it to full-order $\bar{\mathbf{F}}_{\Gamma^{\text{fs}}} = \{\bar{\mathbf{F}}_{\Gamma^{\text{fs}}}^1 \bar{\mathbf{F}}_{\Gamma^{\text{fs}}}^2 \dots \bar{\mathbf{F}}_{\Gamma^{\text{fs}}}^n\}$ and still maintaining a lower DL grid resolution. This is achieved by constructing the functional recovery mapping Ψ . We select the coarse grid $N_x \times N_y \times N_z$ that recovers these bulk force quantities with Ψ mapping by avoiding the need of super-resolution. The process of constructing the Ψ mapping is summarised as:

- Get the voxel forces $\bar{\mathbf{F}}_b = \{\bar{\mathbf{F}}_b^1 \bar{\mathbf{F}}_b^2 \dots \bar{\mathbf{F}}_b^n\}$ and full-order forces $\bar{\mathbf{F}}_{\Gamma^{\text{fs}}} = \{\bar{\mathbf{F}}_{\Gamma^{\text{fs}}}^1 \bar{\mathbf{F}}_{\Gamma^{\text{fs}}}^2 \dots \bar{\mathbf{F}}_{\Gamma^{\text{fs}}}^n\}$ for n training time steps,
- Define the the mean and fluctuating force components

$$\begin{aligned} \bar{\mathbf{F}}_b' &= \bar{\mathbf{F}}_b - \text{mean}(\bar{\mathbf{F}}_b), \\ \bar{\mathbf{F}}_{\Gamma^{\text{fs}}} &= \bar{\mathbf{F}}_{\Gamma^{\text{fs}}} - \text{mean}(\bar{\mathbf{F}}_{\Gamma^{\text{fs}}}), \end{aligned} \quad (13)$$

- Calculate the time-dependent derivative error \bar{E}_c

$$\bar{E}_c = (\bar{\mathbf{F}}_{\Gamma^{\text{fs}}} - \bar{\mathbf{F}}_b)' / (\bar{\mathbf{F}}_b)', \quad \text{with } \bar{\mathbf{F}}_b' \neq 0, \quad (14)$$

- Reconstruct the voxel forces to full-order with mean and derivative corrections

$$\begin{aligned} \bar{\mathbf{F}}_b &= \bar{\mathbf{F}}_b' + \text{mean}(\bar{\mathbf{F}}_{\Gamma^{\text{fs}}}) + \text{mean}(\bar{E}_c) \bar{\mathbf{F}}_b', \\ &= \Psi \bar{\mathbf{F}}_b'. \end{aligned} \quad (15)$$

This mesh-to-mesh field transfer and load recovery process brings uniformity in the field information to coarse-grain the full-order information. It also recovers the interface information together with convenience in training the CRAN driver.

IV. DEEP LEARNING-BASED REDUCED ORDER MODELING FRAMEWORK

We present a hybrid DL-ROM framework that can be trained with variable Re -based full-order unsteady information on a range of 3D flow patterns. In conjunction with a 3D convolutional autoencoder for the dimensionality reduction, we use the well-known LSTM-RNNs for evolving the low-dimensional states in time. The LSTM-RNN represents a mathematical framework that depicts a nonlinear state-space form, making it suitable for nonlinear dynamical systems. When the low-dimensional states are obtained using a 3D convolutional autoencoder and evolved in time with the LSTM-RNN, the hybrid framework is called the 3D CRAN.

We use an approach known as transfer learning to efficiently learn and predict variable Re -based unsteady flow for a 3D CRAN. Transfer learning is the process of improving learning in a new task by transferring knowledge from a previously learned related task. The CRAN architecture learns the task of time series prediction for single Re -based flow information with a remarkable accuracy. The goal of transfer learning is to improve learning in the variable Re -based flow by leveraging knowledge from the single Re -based flow task. We next elaborate a brief description of 3D CNNs, formulation of our 3D hybrid DL-ROM framework and its integration with transfer learning for predicting variable Re -based unsteady flow in time.

A. 3D convolutional neural networks

In this study, we consider 3D convolutional neural networks for our hybrid DL-ROM technique. They are utilized to extract relevant features from the 3D unsteady flow data to construct the reduced-order state. The application of 2D CNNs as a reduced-order model has been explored by Miyawala and Jaiman³⁸ to predict bluff body forces. For the sake of explanation, we briefly describe the feature extraction process of a 3D CNN that is useful for constructing the encoder network of the convolutional autoencoder. Analogous to a 2D operation, a 3D CNN layer takes a set of vectors as input and applies the discrete convolutional operation. This is achieved via a number of 3D kernels as shown using the blue arrows in Fig. 3.

For the first 3D convolution operation, the input is the flow field snapshot: $\mathbf{S}^n \in \mathbb{R}^{N_x \times N_y \times N_z}$. For simplicity, let us denote this input using $D(x, y, z)$. For any L^{th} convolutional layer, let k_L denote the number of feature kernels. We group these kernels of size $f_x \times f_y \times f_z$ into a 4D tensor $K^L \in \mathbb{R}^{f_x \times f_y \times f_z \times k_L}$. When we apply the first operation of 3D convolution on the input matrix, i.e. $L = 1$, it generates a 4D tensor $Y^{C1} = \{Y_{ijkl}^{C1}\}$

$$\begin{aligned} Y_{ijkl}^{C1} &= D_{ijk} \star K_{ijkl}^1, \\ &= \sum_{c=1}^{N_z} \sum_{b=1}^{N_y} \sum_{a=1}^{N_x} D_{abc} K_{(i-a+1)(j-b+1)(k-c+1)l}^1, \end{aligned} \quad (16)$$

where $l = 1, 2, \dots, k_L$. The \star sign represents the convolutional

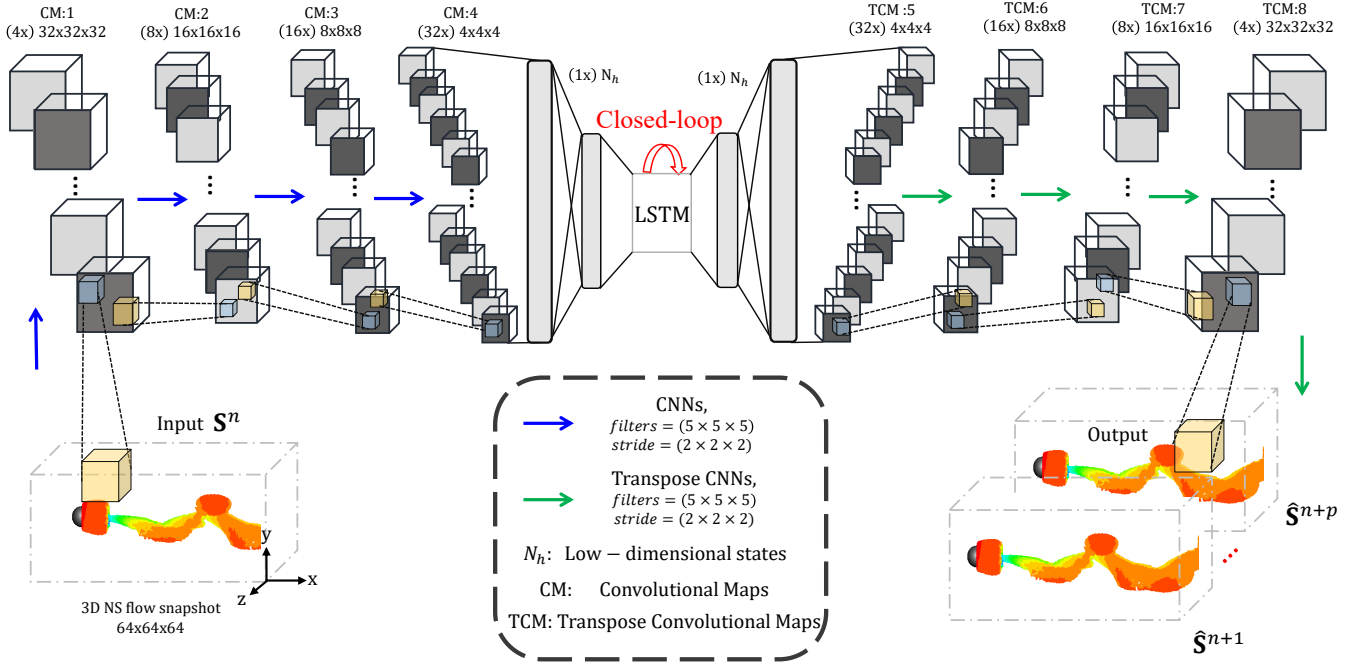


FIG. 3: Schematic of the 3D CRAN framework for unsteady flow predictions. The encoding is constructed by utilising 3D CNNs to reduce the input dimension, and the decoding is achieved by using transpose 3D CNNs. The LSTM-RNN evolves the low-dimensional states between the encoder and decoder networks.

process, which allows local features to be extracted from a 3D space. Eq. (16) is modified slightly if the convolutional blocks are skipped on more than one element of the input function along any cartesian direction.

The skipping lengths along the three directions of the input is termed as the stride $s_L = [s_x \ s_y \ s_z]$ and is an important hyperparameter for the dimensionality reduction. For the 3D CNN operation of the CRAN architecture, we utilize a filter length $(f_x \times f_y \times f_z) = (5 \times 5 \times 5)$ and stride $s_L = [2 \ 2 \ 2]$. The input to the convolutional layer is a 4D tensor, except for the input layer. The L^{th} layer takes each 3D slice of the tensor $Y^{C(L-1)}$ and convolutes them with all the kernels which create a 4D tensor Y^{CL} . Because convolution is a linear operation, a nonlinearity must be introduced in this process to capture complicated nonlinear flow features such as vortex patterns. We employ the sigmoid activation $\sigma(z) = (1 + e^{-z})^{-1}$ function for this purpose. We next briefly review the 3D CRAN framework which utilizes these 3D CNNs to construct the low-dimensional states and infer 3D fields in time.

B. 3D convolutional recurrent autoencoder network

This projection and propagation technique extracts the low-dimensional encoding of the flow variables by using 3D CNNs. The obtained low-dimensional states are propagated in time using the LSTM-RNN to evolve the encoding. We build a decoding space of 3D transpose convolutions that up-samples the low-dimensional encoding back to the high-dimensional space to decode the evolving features. It is assumed that the

3D unsteady flow solutions draw a low-dimensional subspace, allowing an embedding in the high-dimensional space. The end-to-end three-dimensional convolutional recurrent autoencoder architecture is illustrated in Fig. 3.

The 3D CRAN framework relies on the high-fidelity snapshots of flow field acquired from the full-order simulation. Let $\mathbf{S} = \{\mathbf{S}^1 \ \mathbf{S}^2 \ \dots \ \mathbf{S}^n\} \in \mathbb{R}^{N_x \times N_y \times N_z \times n}$ denote the 3D snapshots of any field dataset. $\mathbf{S}^i \in \mathbb{R}^{N_x \times N_y \times N_z}$ indicates a field snapshot and n represents the number of such snapshots. As described in section III, N_x , N_y and N_z represent the number of data probes in the respective Cartesian axes for the uniform voxel grid. For the present case, $N_x = N_y = N_z = 64$. The target of the CRAN-based data-driven prediction is to encode-evolve-decode to the future values at the field probes: $\hat{\mathbf{S}}^{n+1}, \hat{\mathbf{S}}^{n+2}, \dots, \hat{\mathbf{S}}^{n+p}$ for some finite time steps. For the sake of clarity, let us assume that \mathbf{S} is a dataset matrix consisting of time series information for a single Re flow field obtained from the Navier-Stokes solver. The preparation of the dataset matrix for variable Re is straightforward and is described later in section IV C.

1. Proposed architecture

Using the 3D encoder-decoder architecture of the convolutional autoencoder, the low-dimensional states $\mathbf{A}_c = \{\mathbf{A}_c^1 \ \mathbf{A}_c^2 \ \dots \ \mathbf{A}_c^n\} \in \mathbb{R}^{h \times n}$ of the full-order dataset \mathbf{S} are determined in an unsupervised manner. The nonlinear encoding

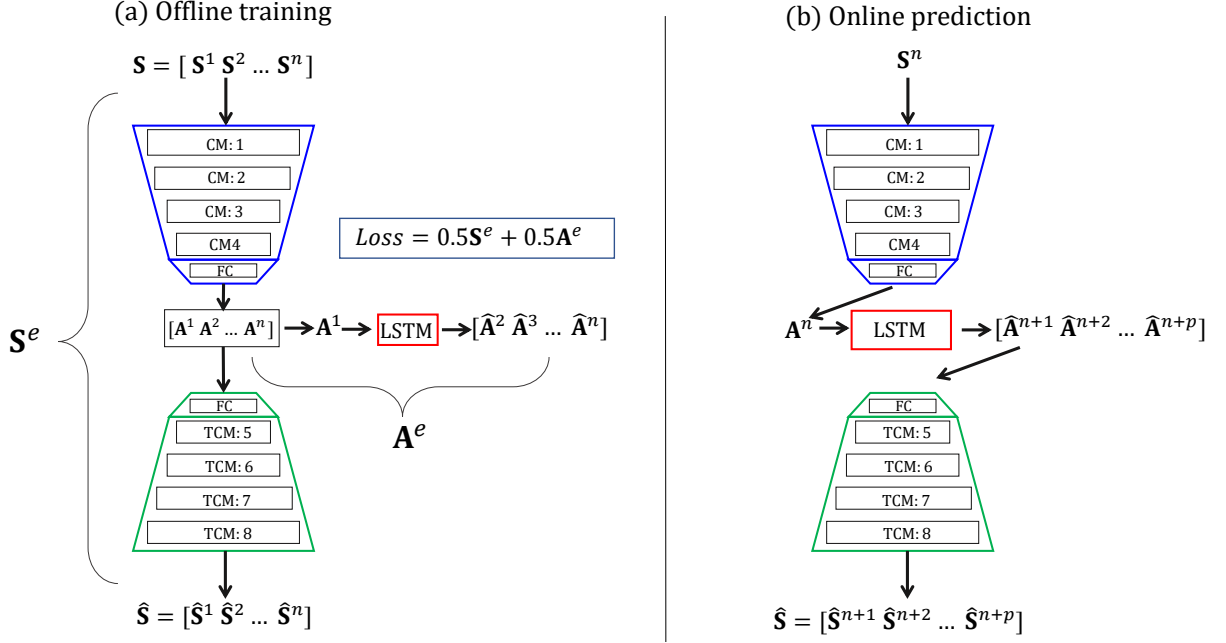


FIG. 4: Illustration of the training and prediction process of the CRAN architecture. (a) An offline training strategy for the 3D CRAN. (b) Iterative process of online predictions using the 3D CRAN. Refer to all the variable details in section IV B.

feature space can be expressed as

$$\mathbf{A}_c^i = f_{enc}(\mathbf{S}^i; \theta_{enc}), \quad i = 1, 2, \dots, n, \quad (17)$$

where f_{enc} is a compositional function consisting of a trainable encoder space that is parametrized by θ_{enc} . As shown in Fig. 3, f_{enc} consists of four blocks of 3D convolutional layers followed by plain vanilla feed forward networks to return a vectorized feature map $\mathbf{A}_c^i \in \mathbb{R}^h$. Unlike the energy or orthogonality constraint of the linear POD-Galerkin, the convolutional autoencoder automatically reduces the order of high-dimensional field from $O(N_x \times N_y \times N_z)$ to $O(h)$ via a nonlinear manifold projection. $h < n \ll N_x \times N_y \times N_z$ and h is usually an unknown hyperparameter for the optimal feature extraction based on the input dataset \mathbf{S} .

LSTM networks are employed to model the evolution of the low-dimensional states. Using a one-to-one dynamic transformation g_{lstm} , the LSTM evolver maps the low-dimensional states $\{\mathbf{A}_c^1, \mathbf{A}_c^2, \dots, \mathbf{A}_c^{n-1}\}$ to the time advanced low-dimensional states $\{\hat{\mathbf{A}}_c^2, \hat{\mathbf{A}}_c^3, \dots, \hat{\mathbf{A}}_c^n\}$ in a closed-loop recurrent manner.

$$\hat{\mathbf{A}}_c^i = g_{lstm}(\mathbf{A}_c^{i-1}; \theta_{lstm}), \quad i = 2, \dots, n, \quad (18)$$

where θ_{lstm} represents the weight operators of the LSTM cell. Notably, in the current work, a single layer LSTM network is found to be sufficient for evolving the feature vectors \mathbf{A}_c obtained from the 3D snapshots. The process of 3D transpose convolutions is carried out via the last four layers of the 3D CRAN and is depicted using the green arrows in Fig. 3. The 3D transpose convolution can be interpreted as the mirror of 3D convolution that upsamples/decodes the low-dimensional representations across four layers to reconstruct the high-dimensional state. For an evolved low-dimensional

state $\hat{\mathbf{A}}_c^{n+1}$, the decoder compositional function of the 3D CRAN can be expressed using

$$\hat{\mathbf{S}}^{n+1} = f_{dec}(\hat{\mathbf{A}}_c^{n+1}; \theta_{dec}), \quad (19)$$

where f_{dec} is the trainable decoder space that is parametrized by θ_{dec} and $\hat{\mathbf{S}}^{n+1}$ is a predicted high-dimensional 3D field. The end-to-end 3D CRAN on flow variables is unsupervised and is capable of predicting flow variables at fixed 3D probes as long as the prediction error is within an acceptable range of accuracy.

2. Training and prediction:

The snapshot dataset matrix \mathbf{S} is normalised and batch-wise arranged for ease in training. By subtracting the temporal mean from the dataset matrix and scaling the fluctuations, the dataset matrix is first normalized. The resultant dataset is rearranged into a set of N_s finite time training sequences, where each sequence consists of N_t snapshots. This data processing converts the snapshot matrix \mathbf{S} into a 5D tuple of the following form:

$$\mathcal{S} = \{\mathcal{S}_s^1, \mathcal{S}_s^2, \dots, \mathcal{S}_s^{N_s}\} \in [0, 1]^{N_x \times N_y \times N_z \times N_t \times N_s}, \quad (20)$$

where each training sample $\mathcal{S}_s^j = [\mathbf{S}_{s,j}^1, \mathbf{S}_{s,j}^2, \dots, \mathbf{S}_{s,j}^{N_t}]$ is a matrix consisting of the scaled database and each $\mathbf{S}_{s,j}^i \in [0, 1]^{N_x \times N_y \times N_z}$ is a normalized 3D flow snapshot.

We utilize an unsupervised-supervised training strategy to train the CRAN architecture as there are two types of losses

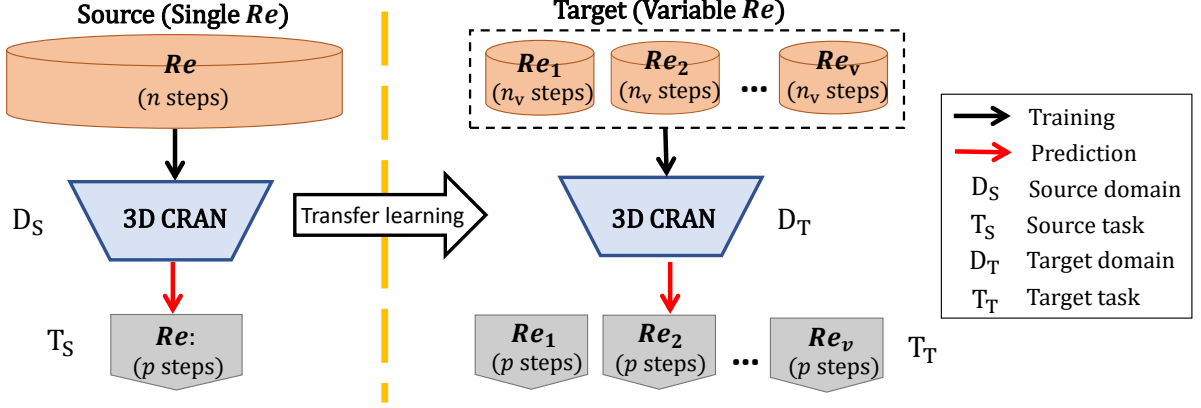


FIG. 5: Illustration of the transfer learning process for training variable Re flows. Source refers to learning and extrapolating single Re flows in time. Target refers to learning and extrapolating multiple Re flows in time. Note that for training steps $n_v < n$.

obtained in a CRAN. One is the unsupervised loss accounted for the 3D convolutional autoencoder reconstruction \mathbf{S}^e and the other is the supervised loss \mathbf{A}^e obtained from the evolution of the low-dimensional representations using the LSTM. This can be clarified from Fig. 4(a). A hybrid loss function E_h is constructed that equally weights the error in the unsupervised and supervised losses of the CRAN. The target of the training is to find the CRAN parameters $\theta = \{\theta_{enc}, \theta_{dec}, \theta_{lstm}\}$ such that for any sequence $\mathcal{S}_s^j = [\mathbf{S}_{s,j}^1, \mathbf{S}_{s,j}^2, \dots, \mathbf{S}_{s,j}^{N_t}]$ and its corresponding low-dimensional representation $[\mathbf{A}_{c,j}^1, \mathbf{A}_{c,j}^2, \dots, \mathbf{A}_{c,j}^{N_t}]$ the hybrid loss E_h is minimized:

$$\begin{aligned} \theta &= \operatorname{argmin}_{\theta}(E_h), \\ &= \operatorname{argmin}_{\theta}(0.5\mathbf{S}^e + 0.5\mathbf{A}^e). \end{aligned} \quad (21)$$

Here, \mathbf{S}^e and \mathbf{A}^e are given using the following expressions:

$$\begin{aligned} \mathbf{S}^e &= \frac{1}{N_t} \sum_{i=1}^{N_t} \frac{\left\| \mathbf{S}_{s,j}^i - f_{dec}(f_{enc}(\mathbf{S}_{s,j}^i; \theta_{enc}); \theta_{dec}) \right\|_2^2}{\left\| \mathbf{S}_{s,j}^i \right\|_2^2}, \\ \mathbf{A}^e &= \frac{1}{N_t - 1} \sum_{i=2}^{N_t} \frac{\left\| \mathbf{A}_{c,j}^i - g_{lstm}(\mathbf{A}_{c,j}^i; \theta_{lstm}) \right\|_2^2}{\left\| \mathbf{A}_{c,j}^i \right\|_2^2}. \end{aligned} \quad (22)$$

The hybrid loss function given by Eqs. (21)-(22) is minimized over all the $j = 1, 2, \dots, N_s$ training sequences using the adaptive moment optimization³³.

The online prediction is straight forward and is depicted in Fig. 4(b) for easy comprehension. The low-dimensional representation $\mathbf{A}_c^n \in \mathbb{R}^h$ is constructed using the encoder network for a given initial 3D flow snapshot $\mathbf{S}^n \in [0, 1]^{N_x \times N_y \times N_z}$ and the trained 3D CRAN parameters θ . Eq. (18) is applied iteratively for p steps with $\mathbf{A}_c^n \in \mathbb{R}^h$ as the initial solution to generate predictions of the low-dimensional representations $\hat{\mathbf{A}}_c = \{\hat{\mathbf{A}}_c^{n+1}, \hat{\mathbf{A}}_c^{n+2}, \dots, \hat{\mathbf{A}}_c^{n+p}\}$. Finally, the 3D state is reconstructed from the low-dimensional representations at every

time steps using the decoder network. We next detail the formulation of the training strategy for the 3D CRAN for variable Re -based flows using transfer learning.

C. Variable Re -based flows

As discussed in the previous section, scaling the CRAN to 3D is algorithmically straightforward as the framework largely relies on 3D CNNs to extract the flow features. However, this simple algorithmic extension can considerably increase the memory requirement, hyperparameter space, and training costs for the end-to-end learning model. In some cases, the offline training time for learning a simple flow regime can take a matter of days or weeks if the CRAN framework starts learning from scratch. This often results in: (a) enormous computing power for training than the full-order model itself and, (b) large training data requirement for the neural network. These challenges can complicate the process of training a 3D CRAN-based framework, especially for learning complex flow patterns involving variable Re -based flows.

To overcome these challenges, transfer learning is beneficial. Transfer learning, employed in machine learning, refers to the use of a previously trained network to learn a new task. In transfer learning, a machine uses a previously learned task to increase generalisation about another. The neural parameters and task for a pre-trained network are called as the source domain and source task, respectively. Whereas, the neural parameters and task for a new network are called as the target domain and target task, respectively. This is further elaborated in Fig. 5. For a source domain D_S with a corresponding source task T_S and a target domain D_T with a corresponding task T_T , transfer learning is the process of improving the target CRAN predictive function by using the related information from D_S and T_S , where $D_S \neq D_T$ or $T_S \neq T_T$. The single source domain defined here can be extended to multiple target domains or tasks. This study employs transfer learning to

train the 3D CRAN for a variable Re flow regime on a limited data and training time. For this purpose, we load a pre-trained model of a single Re case and optimize for variable Re flows. The source domain and task are to learn and predict single Re flows in time using 3D CRAN. On the flip side, the target domain and task become learning and prediction of multi- Re flows in time using one 3D CRAN.

1. Training and prediction

We use the same 3D CRAN architecture and, training and prediction algorithms for variable Re flows as described in section IV B. The only difference is the preparation of the dataset matrix. For variable Re flows, the time series data are snapshots of flow fields for different Re values acquired from the full-order simulation. Consider that $Re_m = [Re_1 Re_2 \dots Re_v]$ be the range of Reynolds number for generating the full-order fields. The training dataset matrix $\mathbf{S}(Re_m)$ consists of time series data for different Re fields (pressure or velocity) that are stacked as a matrix

$$\mathbf{S}(Re_m) = \begin{Bmatrix} [\mathbf{S}^1(Re_1) \ \mathbf{S}^2(Re_1) \ \dots \ \mathbf{S}^{n_v}(Re_1)], \\ [\mathbf{S}^1(Re_2) \ \mathbf{S}^2(Re_2) \ \dots \ \mathbf{S}^{n_v}(Re_2)], \\ \vdots \\ [\mathbf{S}^1(Re_v) \ \mathbf{S}^2(Re_v) \ \dots \ \mathbf{S}^{n_v}(Re_v)] \end{Bmatrix}. \quad (23)$$

Note that $\mathbf{S}(Re_m) \in \mathbb{R}^{N_x \times N_y \times N_z \times (v n_v)}$ consists of v Reynolds numbers and each consisting n_v snapshots. $N_x = N_y = N_z = 64$ represents the number of data probes for the uniform voxel grid. The training dataset matrix is normalised and batch-wise arranged for ease in training. The matrix re-arranges in the following form

$$\mathcal{S}(Re_m) = \{ \mathcal{S}_s^1 \ \mathcal{S}_s^2 \ \dots \ \mathcal{S}_s^{N_s} \} \in [0, 1]^{N_x \times N_y \times N_z \times N_t \times N_s}, \quad (24)$$

where each training sample $\mathcal{S}_s^j = [\mathbf{S}_{s,j}^1 \ \mathbf{S}_{s,j}^2 \ \dots \ \mathbf{S}_{s,j}^{N_t}]$ is a time series data at a particular Re value. N_t are the evolver steps while N_s are the number of batches. While training, sequence of different Re field is selected randomly $\mathcal{S}_s^j \subset \mathcal{S}(Re_m)$ to optimize the loss function given by Eqs. (21)-(22).

The prediction algorithm is the same as illustrated in Fig. 4(b). For a given initial 3D flow snapshot $\mathbf{S}^{n_v}(Re_i) \in [0, 1]^{N_x \times N_y \times N_z}$ at a Reynolds number say $Re_i \subset Re_m$, the trained 3D CRAN parameters and Eq. (18) is applied iteratively for p steps with $\mathbf{A}_c^{n_v}(Re_i) \in \mathbb{R}^h$ as the initial solution. This helps to infer multiple- Re fields in time for a chosen value of Re_i . With transfer learning, a 3D CRAN model can be built with comparatively less training data and time because the model is already pre-trained. This can be valuable in tasks where the data can be limited and unlabeled, for instance variable Re flows.

V. RESULTS AND DISCUSSION

In this section, we test our proposed 3D snapshot-FTLR and DL-ROM methodologies for data-driven prediction of flow

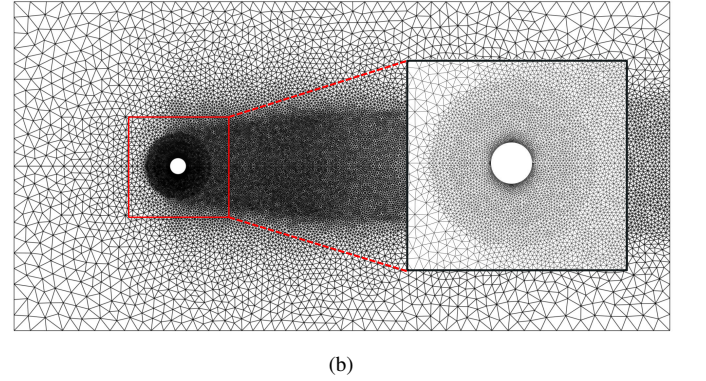
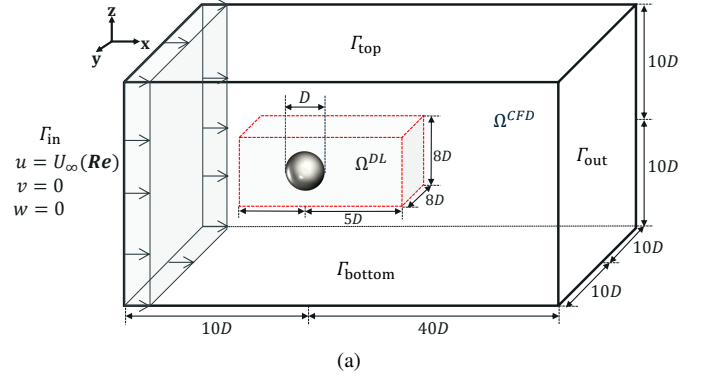


FIG. 6: (a) Schematic and associated boundary conditions of flow past a sphere and deep learning domain of interest. (b) Representative CFD mesh for the entire domain sliced in $Z/D = 10$ plane.

past a sphere. We are interested in integrating an end-to-end 3D spatial encoding-decoding and temporal evolution for a realistic CFD problem with usual boundary conditions. Of particular interest is to forecast flow fields for single and variable Re flow information in the DL space using an optimized CRAN framework, while preserving the interface description from the voxel grid.

A schematic of the problem configuration employed for the full-order data generation Ω^{CFD} , of a stationary mounted sphere, is shown in Fig 6 (a). The sphere system of diameter D is installed in the 3D computational domain of size $50D \times 20D \times 20D$, with center at sufficient distances from the far-field boundaries to capture the downstream sphere wake. u , v and w depict the streamwise, transverse and vertical flow velocities in the x , y and z directions, respectively. A uniform free-stream velocity profile $\{u, v, w\} = \{U_\infty, 0, 0\}$ is maintained at the inlet boundary (Γ_{in}). Here, the free stream velocity is adjusted by defining the Re of the problem using $Re = \rho^f U_\infty D / \mu^f$, with ρ^f and μ^f being the fluid density and viscosity, respectively. Along the top Γ_{top} , bottom Γ_{bottom} , and side surfaces, a slip-wall boundary condition is implemented while a traction-free Neumann boundary is maintained on the outlet Γ_{out} . The streamwise C_x , the transverse C_y and the vertical force coefficients C_z on the submerged sphere are calculated by integrating the Cauchy stress tensor σ^f on the sphere

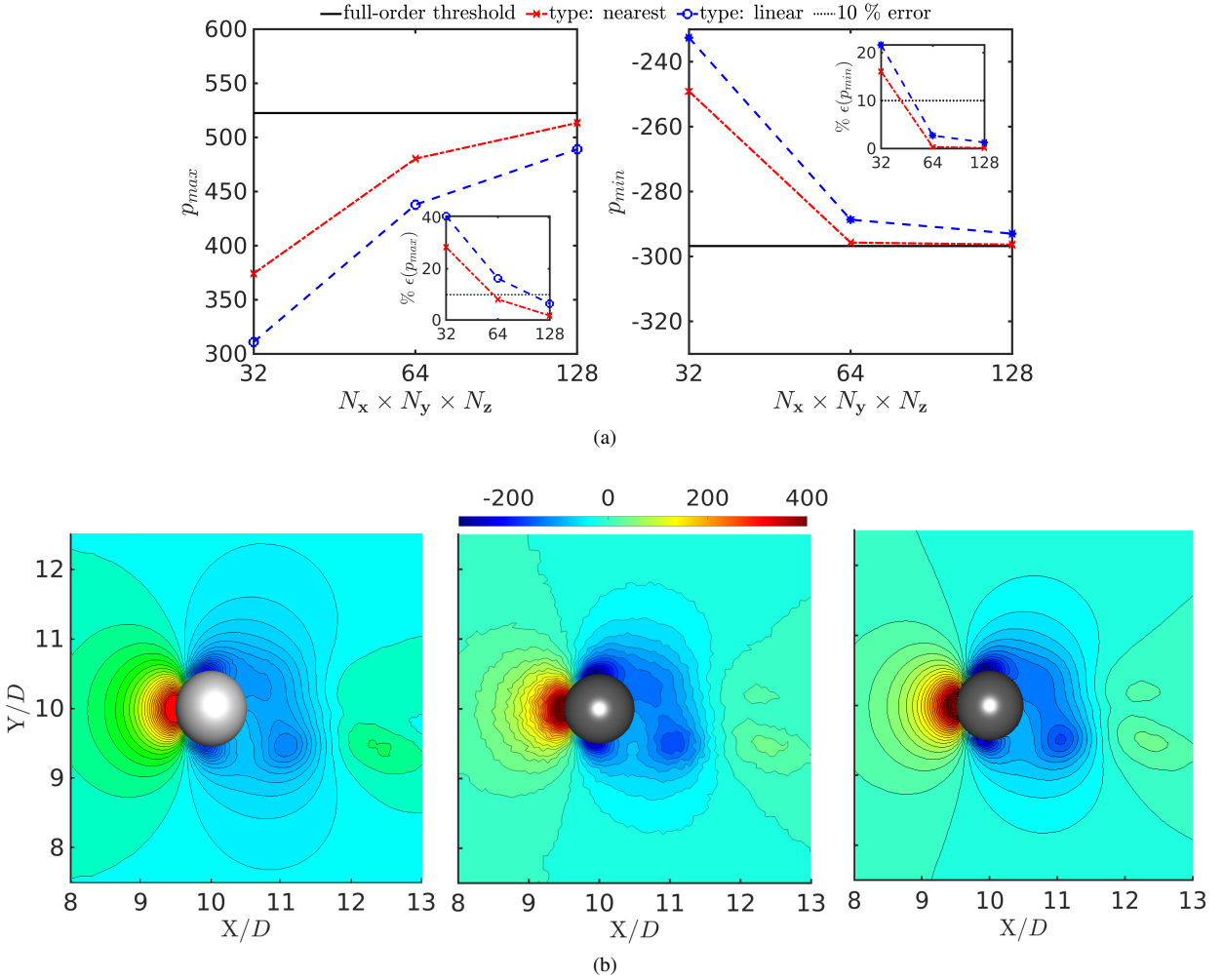


FIG. 7: The flow past a sphere: (a) Pressure field convergence with number of flow voxels for interpolation scheme variants. $\epsilon(\cdot)$ is the respective relative error. (b) Descriptive behaviour of nearest-neighbour (middle) and linear interpolation (right) techniques for pressure field in the DL space $128 \times 128 \times 128$ with respect to CFD space (left) sliced at $Z/D = 10$. Plots correspond to $tU_\infty/D = 200$.

Γ^{fs} using Eq. (6).

In the following sub-sections, we apply the 3D snapshot-FTLR and CRAN methodologies for synchronously predicting the flow fields and the pressure force coefficients, by selecting a DL domain of interest Ω^{DL} as shown in Fig. 6 (a).

A. Flow past sphere at constant Re

To assess the 3D flow reconstruction and coarse-grain field predictions, we first examine our 3D data-driven DL-ROM framework on an unsteady fully submerged sphere problem in external flow at a single Re . The objective, herein, is to learn the strength and shedding orientation of unsteady planar-symmetric flow at $Re = 300$, where the downstream hair-pinned shaped vortices shed strongly periodic in the near sphere wake. The drag C_x and total lift $C_L = \sqrt{C_y^2 + C_z^2}$ coefficients demonstrate periodic behavior pattern from $tU_\infty/D \approx$

TABLE I: The flow past a sphere: The present study's full-order force values compared to benchmark data. \bar{C}_D and \bar{C}_L represent the mean drag and lift force coefficients, respectively. St is the Strouhal number.

Study	\bar{C}_D	\bar{C}_L	St
Present	0.669	0.082	0.137
Johnson and Patel ²⁹	0.656	0.069	0.137

200 onward. The full-order unsteady flow simulation is first carried out in the unstructured CFD domain to generate the full-order data. We use a time step of $\Delta t = 0.05 tU_\infty/D$ for a total of $400 tU_\infty/D$ at $Re = 300$. The final mesh is obtained using standard principles of mesh convergence and the full-order output details are tabulated in Table I to validate the FEM solver.

A total of 1600 time snapshots of point cloud data are saved

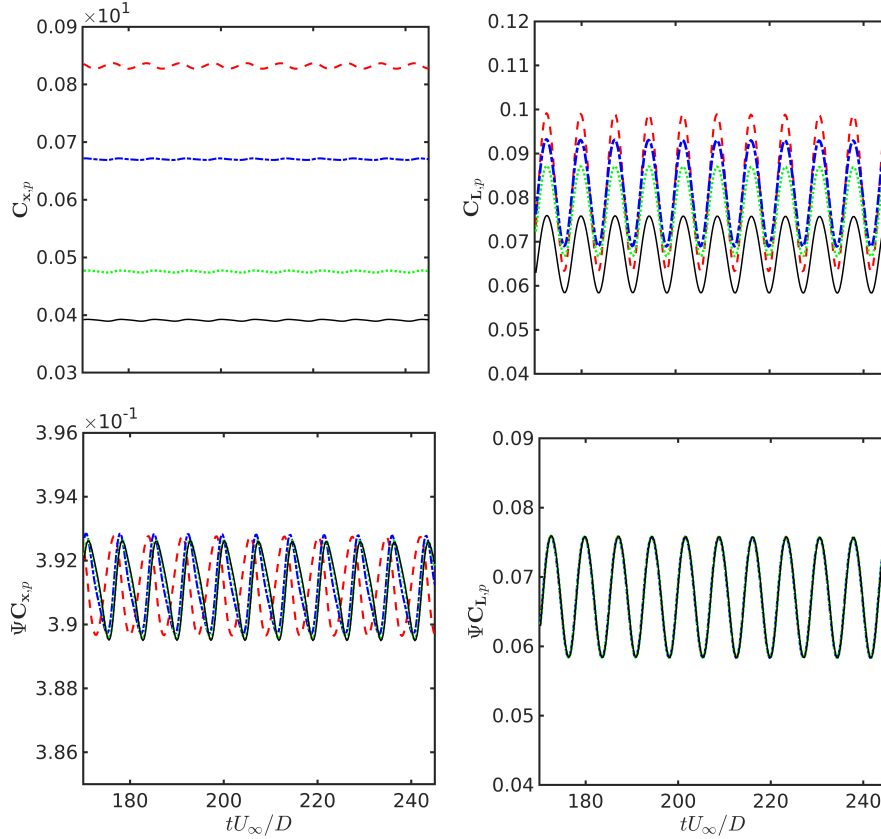


FIG. 8: The flow past a sphere: Voxel interface force propagation and load recovery effects on various snapshot 3D DL grids (shown from 170-245 tU_{∞}/D). Voxel drag and lift components (Row 1). Corresponding voxel force recovery (Row 2). Red, blue and green dashed lines represent the grid $32 \times 32 \times 32$, $64 \times 64 \times 64$ and $128 \times 128 \times 128$, respectively. The black line depicts the full-order force.

at every $0.25 tU_{\infty}/D$ for the pressure and x-velocity field. From these full-order data, $n = 1000$ snapshots (from 95-345 tU_{∞}/D) are kept for training and $n_{ts} = 100$ (from 345-370 tU_{∞}/D) are reserved for testing. Thus, the total time steps in this analysis are $N = 1100$. We further organize the test data in groups of every $p = 20$ time steps to assess the compounding error effects in the multi-step predictions from the 3D CRAN solver. After generating the full-order point cloud dataset, we apply the 3D CRAN framework to forecast the flow fields past a sphere in a DL-based voxel grid for $Re = 300$ while preserving the exact interface description.

We employ the snapshot-FTLR to bring field uniformity in the DL space, while recovering forces as described in section III. A DL space Ω^{DL} of dimension $8D \times 8D \times 8D$ is selected with $\approx 5D$ length kept for downstream sphere wake as shown in Fig. 6(a). The point cloud CFD training/testing data (for instance pressure field) $\mathbf{s} = \{\mathbf{s}^1 \mathbf{s}^2 \dots \mathbf{s}^N\} \in \mathbb{R}^{m \times N}$ is interpolated and projected as spatially uniform 3D snapshots $\mathbf{S} = \{\mathbf{S}^1 \mathbf{S}^2 \dots \mathbf{S}^N\} \in \mathbb{R}^{N_x \times N_y \times N_z \times N}$ in the chosen DL space. N_x , N_y and N_z are number of flow voxels in the x, y and z directions, respectively. The field uniformity reduces the model-order fidelity and unstructured mesh complexity by mapping the m -dimensional unstructured dataset on a 3D reference grid. We compare the field interpolation methods pro-

vided by *griddata*¹: nearest and linear methods, with respect to the number of flow voxels. This is performed by sampling the field's maximum and minimum values for various 3D DL grid resolution at an instant $tU_{\infty}/D = 200$. On DL grid refinement, the nearest method levels-off to the true p_{max} and p_{min} for a pressure instant as illustrated in Fig. 7(a). Because this method assigns the value of the nearest neighbour in the unstructured information, this effect is expected. The linear interpolation approach, however, linearly converges p_{max} and p_{min} to the true full-order values on grid refinement.

Fig. 7(b) compares the field interpolation methods for pressure field with respect to the full-order on a $128 \times 128 \times 128$ DL voxel grid. The presence of the sphere boundary is ensured by masking the exact interface description in the 3D DL grid. It can be interpreted that, because of a discontinuous assignment of fields at the specified probes, the nearest method contains oscillations compared to the full-order description. With the linear interpolation and projection, a nearly perfect match is obtained in terms of the descriptive near wake snapshot ($\epsilon(p_{max}) \approx 7\%$, $\epsilon(p_{min}) \approx 2\%$) devoid of noises. The qualitative description is further substantiated by the convergence behavior in Fig. 7(a). Hence, we rely on the linear interpolation technique for 3D coarse-grain field assignment.

The total voxel force propagation (drag and lift force com-

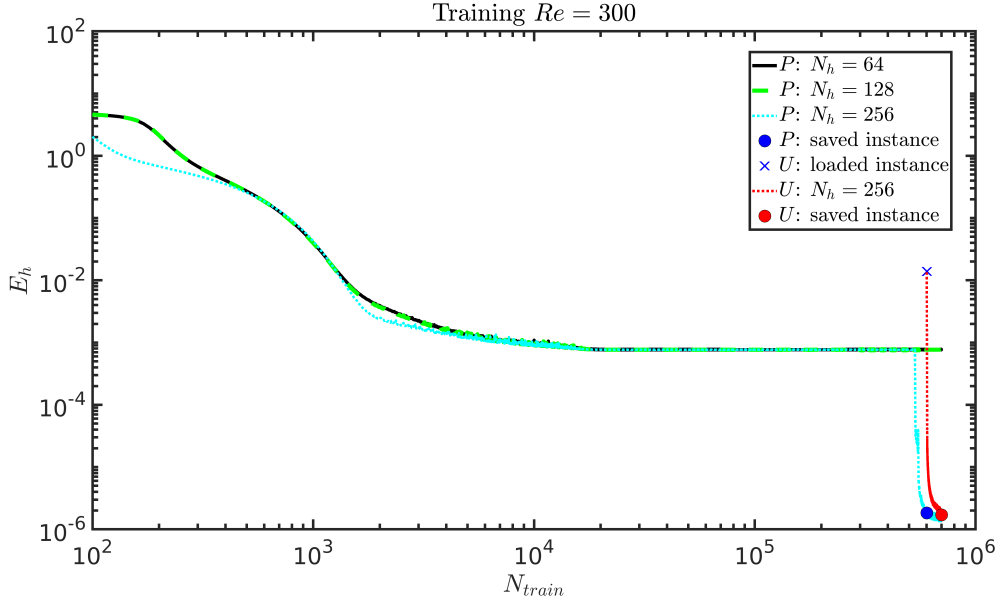


FIG. 9: The flow past a sphere: Evolution of the loss function E_h with training iterations for different evolver cell sizes N_h . P and U denote the 3D CRAN trained with pressure and x-velocity datasets, respectively. Blue and red dots depict the saved instances for testing the pressure and x-velocity fields, respectively. The blue cross represents the initialization of velocity training from saved pressure parameters.

ponents) $\bar{\mathbf{F}}_b = \{\bar{\mathbf{F}}_b^1, \bar{\mathbf{F}}_b^2, \dots, \bar{\mathbf{F}}_b^N\}$ are obtained from the interface voxels on various 3D DL Cartesian grids using Eq. (12). The primary idea is to recover this bulk quantity by a functional corrective mapping Ψ on the chosen DL grid using the exact fluid-solid interface location. Fig. 8 demonstrates the DL grid dependence of normalized pressure voxel forces $\bar{\mathbf{F}}_b/0.5\rho^f U_\infty^2 D$ and their data recovery effects using the mapping Ψ . It can be interpreted that low-resolution leads to mean and derivative errors in the voxel forces compared with the full-order CFD forces. The primary reasons are the considerable loss of boundary fidelity in the DL grid and a linear force calculation using finite difference.

Fig. 8 also depicts the force correction by observing the Ψ mapping and correcting on the training forces. For the flow field predictions using 3D CRAN, we rely on the DL grid $64 \times 64 \times 64$ because it accounts for a reasonable force recovery across all components ($\varepsilon(C_{x,p}) = 0.0019$, $\varepsilon(C_{L,p}) = 0.0026$) without requiring the need of super-resolution. With super-resolution, the voxel force errors are indeed decreased. However, we want to refine the DL grid to the point where the force coefficients can be transformed to the full-order with mean and derivative error quantification using Eqs. (13)-(15). This process facilitates an optimal uniform grid to carry the neural prediction. The snapshot-FTLR procedure is scalable for voxel grid selection so that 3D CNNs can be conveniently integrated with the point cloud full-order dataset.

With the chosen DL grid $N_x = N_y = N_z = 64$, the 3D CRAN is employed for the coarse-grain flow field predictions. The coarse-grain pressure information $\mathbf{S} = \{\mathbf{S}^1 \mathbf{S}^2 \dots \mathbf{S}^N\} \in \mathbb{R}^{N_x \times N_y \times N_z \times N}$ is decomposed into $n = 1000$ learning data (95-345 tU_∞/D) and $n_{ts} = 100$ analysis data (345-370

tU_∞/D). Following this, standard principles of data normalization and batch-wise arrangement are adopted to generate the 5D scaled featured input $\mathcal{S} = \{\mathcal{S}_s^1 \mathcal{S}_s^2 \dots \mathcal{S}_s^{N_s}\} \in [0, 1]^{N_x \times N_y \times N_z \times N_t \times N_s}$ with $N_s = 40$ and $N_t = 25$. The encoding space of the 3D CRAN encodes the $64 \times 64 \times 64$ flow voxel-based input dimension via four layers of 3D CNN operation with a constant kernel size of $5 \times 5 \times 5$ and stride $2 \times 2 \times 2$. Every CNN operation reduces the input size by half, with number filters increasing by twice in every layer. Three feed-forward networks further map the feature vectors until a finite low-dimensional encoding $\mathbf{A}_c \in \mathbb{R}^{N_h}$ is achieved with $N_h \ll N_x \times N_y \times N_z$. The architecture is detailed in section IV B. Since 3D CNNs can considerably increase the trainable variables, the cost of hyperparameter tuning and training is very high. This can result in an increase in computing power for training the framework. Table II depicts a comparison of the computational resources used for the 3D CRAN training and the 2D CRAN⁷. We note that scaling the CRAN architecture to three-dimension increases the trainable parameters by an order magnitude with the increase in random access memory (RAM) and training time.

To train the 3D CRAN, we experiment with different sizes of the evolver cells $N_h = 64, 128, 256$ as primary tuning hyperparameters. In the 3D CRAN, the low-dimensional evolution needs to be tuned for appropriate time series learning and iterative optimization. We start by training each 3D CRAN model on a single v100 graphics processing unit (GPU) on pressure fields by instantiating with random parameter values. These parameters are updated in every training iteration. Every training iteration consists of a mini-batch of size $n_s = 2$ randomly shuffled from the scaled featured flow input \mathcal{S} and updating the neural parameters in $\approx 0.3s$. This helps speed-up

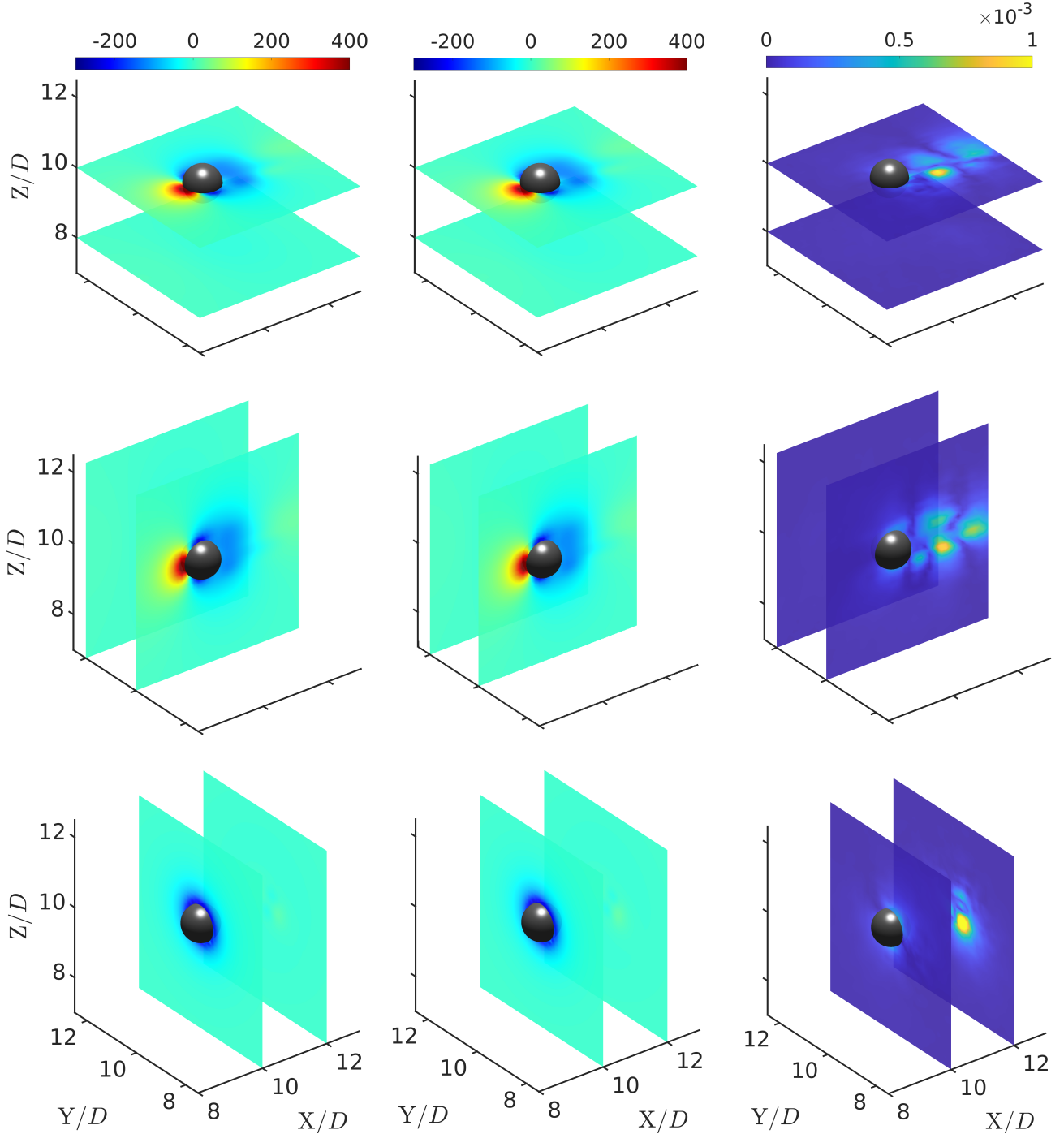


FIG. 10: The flow past a sphere: Predicted and true pressure field comparison along with normalized reconstruction error E^i at $tU_\infty/D = 365$ sliced in $Z/D = (8, 10)$ (Row 1), $Y/D = (10, 12)$ (Row 2), $X/D = (10, 12)$ (Row 3). Left, middle and right contour plots depict the prediction, true and errors, respectively.

the training procedure of the deep 3D CRAN architecture and lower memory usage. The objective function consists of the hybrid loss obtained from the unsupervised-supervised training as detailed in section IV B 2. The evolution of the objective function E_h with the training iterations N_{train} is showcased in Fig. 9.

It can be observed that $N_h = 256$ CRAN model tunes for

the pressure dataset in 6×10^5 training iterations at a loss of 1.74×10^{-6} , which took nearly 64 hours of GPU training. At these training costs and iterations, 3D CRAN models $N_h = 64, 128$, however, do not optimise on the pressure dataset. We save the optimised 3D CRAN model ($N_h = 256$) at $N_{train} = 600800$ on the disc memory as trained parameters. This is shown as blue dot in Fig. 9. To avoid the expensive hy-

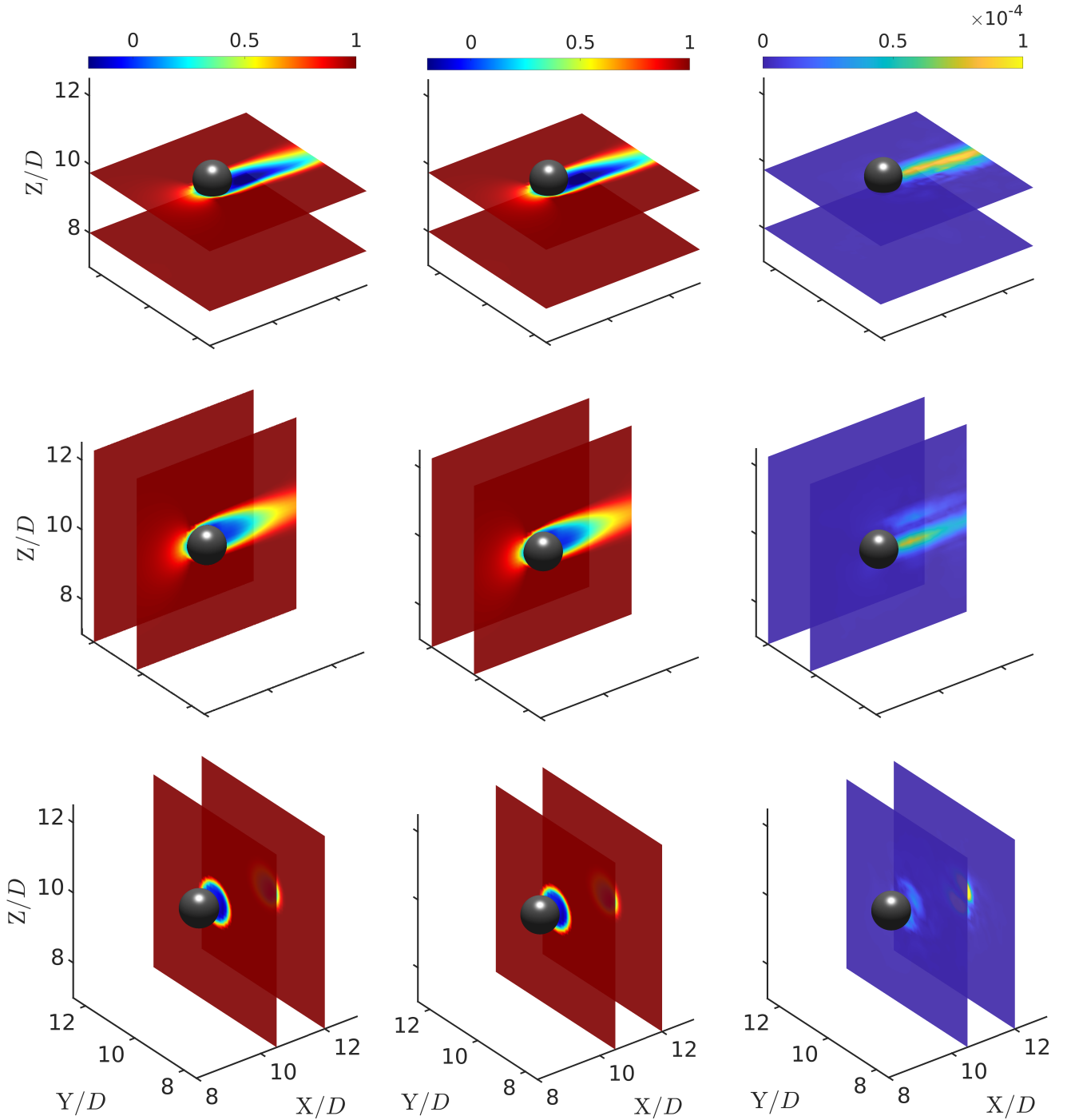


FIG. 11: The flow past a sphere: Predicted and true x-velocity field comparison along with normalized reconstruction error E^t at $tU_\infty/D = 365$ sliced in $Z/D = (8, 9.75)$ (Row 1), $Y/D = (10.25, 12)$ (Row 2), $X/D = (10.5, 12)$ (Row 3). Left, middle and right contour plots depict the prediction, true and errors, respectively.

perparameter search for the velocity field training, we instead load the saved pressure 3D CRAN parameters on the velocity dataset (shown as blue cross) and optimise it further. This transfer of learning depicts that the 3D CRAN model fine-tunes on the coupled velocity dataset and mimics the dynamical model of flow past a sphere. This initialisation of trained

weights to velocity field reduces the training time to nearly 2 hours. We save the x-velocity 3D CRAN model parameters at $N_{train} = 700000$ for velocity testing. This model is depicted by red dot in Fig. 9.

Herein, $N_h = 256$ trained saved instances of the 3D CRAN models are employed to analyze the field predictions for the

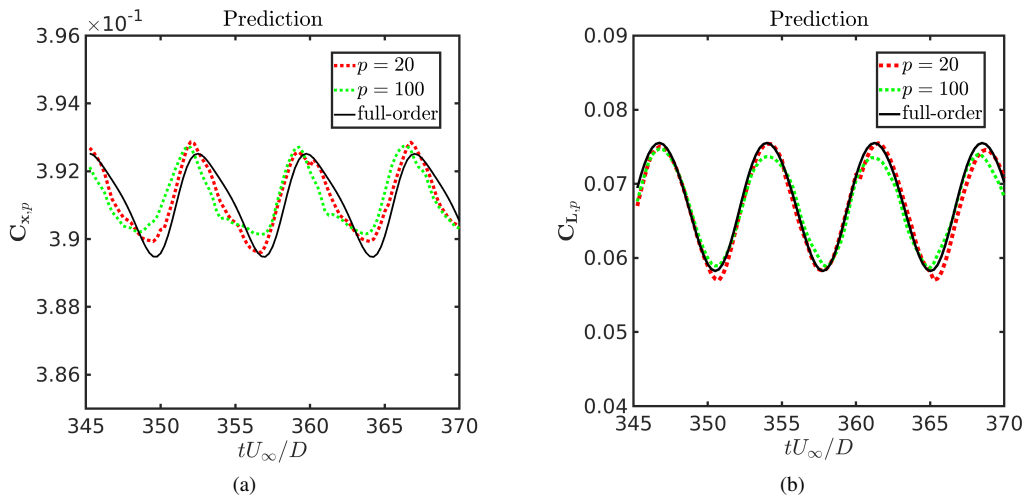


FIG. 12: The flow past a sphere: Predicted and actual (3D CRAN model) (a) drag and (b) lift force coefficients integrated from the predicted pressure field on the sphere for all 100 test time steps with multi-step predictive sequence $p = 20$ and $p = 100$.

TABLE II: Comparison of computational resources used for 3D CRAN and 2D CRAN training.

	3D CRAN (flow past sphere)	2D CRAN ⁷ (flow past cylinder)
DL grid	$64 \times 64 \times 64$	64×64
Training snapshots	$n = 1000$	$n = 1000$
RAM (gB)	32	16
Processor number	Single GPU node	Single CPU node
Processor type	NVIDIA v100	Intel E5 2690
Trainable parameters	$\theta \approx 6 \times 10^6$	$\theta \approx 3 \times 10^5$
Mini-batch size	$n_s = 1 - 2$	$n_s = 2 - 5$
Training time	64 h	16 h

pressure and x-velocity on the test dataset (100 time steps from $345 - 370 tU_\infty/D$). We keep the multi-step predictive cycle length of $p = 20, 100$, implying that one input step infers p sequence of future field predictions until a new input is fed. Figs. 10 and 11 depict a comparison of the predicted and true values of pressure and x-velocity fields, respectively, at $tU_\infty/D = 365$ sliced in various orthogonal planes with $p = 100$. The normalized reconstruction error E^i is calculated by taking the absolute value of the difference between the real and predicted fields and then normalizing it with the truth's L_2 norm. It can be observed that the majority of these errors are located in the nonlinear flow separation region and near-wake of the sphere. These 3D reconstruction errors are in the order of 10^{-3} for pressure and 10^{-4} for x-velocity predictions. This demonstrates the high accuracy of the 3D CRAN for reconstruction and time series extrapolations if properly trained.

The predicted coarse-grain flow fields are directly integrated and corrected using the snapshot-FTLR to get the pressure loads over the sphere. Evolution of the drag $C_{x,p}$ and lift $C_{L,p}$ loads are depicted in Fig. 12. The red line in the

TABLE III: Summary of the offline and online times for 3D CRAN vs. 3D FOM simulations.

	FOM-HPC	3D CRAN-PC
Processor number	32 CPUs	1 GPU
Offline time*	≈ 10 h	≈ 64 h
Online time**	≈ 1 h	≈ 1.99 s
Offline speed-up	1	0.1563
Online speed-up	1	1800

* Elapsed time 1000 training steps.

** Elapsed time 100 test steps.

figure depicts force calculation from pressure fields with sequence prediction length of $p = 20$ steps in a closed-loop recurrence. This helps reduce the compounding effect of the errors with slight improvements compared to $p = 100$ steps predicted from one time instant. In Table III we provide an estimate of the computational costs for the 3D CRAN together with the full-order simulations for flow past a sphere. We recall that the DL-ROM solution can offer remarkable speed-ups in online predictions compared with the FOM by nearly 1800 times. However, the offline training time of 3D CRAN is expensive compared with a similar FOM. The following subsection extends our DL-ROM methodology for predicting unsteady flow fields with variable Re while focusing on speeding up both offline and online computational times.

B. Variable flow past a fixed sphere

As seen previously, a trained 3D CRAN model and snapshot-FTLR offer fast and accurate data-driven field predictions and physical force integration. By fast and accurate, we mean that one can avoid running the full-order model at a specific Re and replace it with an optimized 3D CRAN frame-

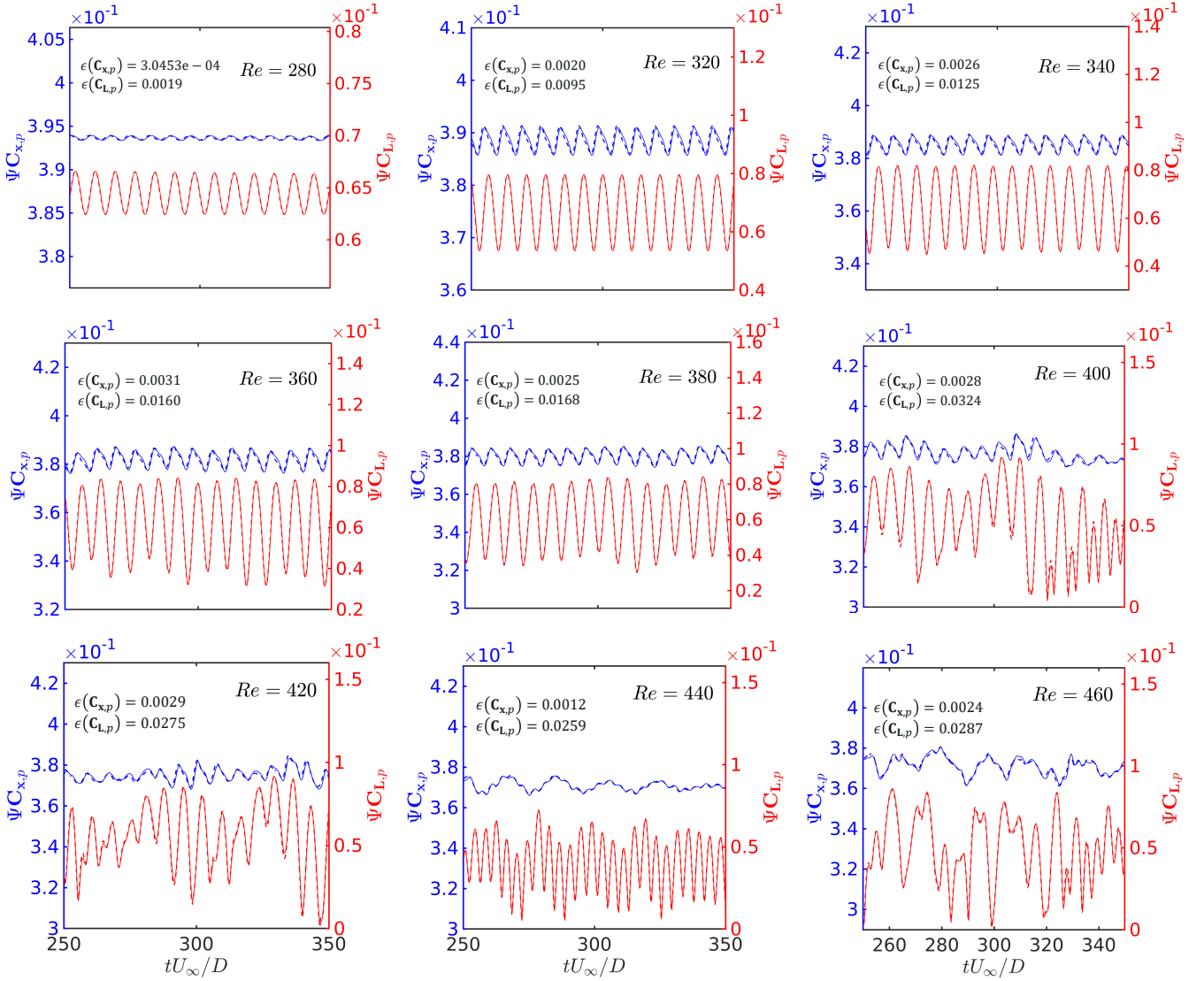


FIG. 13: The variable flow past a sphere: Recovered voxelated load propagation (pressure drag and lift) on DL grid $64 \times 64 \times 64$ vs full-order CFD grid for variable Re flows. Dashed and solid lines indicate the recovered DL grid loads and full-order loads, respectively.

work. However, the major bottleneck of this deep learning architecture is the task of hyperparameter tuning and training, even for learning a periodical vortex shedding phenomenon at constant Re . The expensive offline training for another Re -dependent flow is, hence, less appealing for data-driven prediction from a practical standpoint. Moreover, the training can become challenging in flow scenarios that involve multi- Re information. Subsequently, in this sub-section, we explore the training and predictive abilities of the 3D CRAN framework with multiple Re -based flow patterns. Of particular interest is to optimize a 3D CRAN framework on a variable Re flow dataset within acceptable training cost and accurate predictive abilities.

We start by generating the full-order unsteady point cloud dataset for a variable Re -based 3D flow regime. We utilize the CFD domain in Fig. 6 to generate flow snapshots for $Re_m =$

[280 300 320...460] with a time step $0.25 tU_\infty/D$. For every $Re \in Re_m$, we select a reduced time series training dataset $n_v = 400$ (from 250 till 350 tU_∞/D). However, we maintain the same number of testing dataset $n_{ts} = 100$ (from 350 till 375 tU_∞/D) as compared to a single Re scenario. While the hairpin shaped vortices are periodically shed for the unsteady planar-symmetric flow regime $280 \leq Re \leq 370$, as the Re is increased, the shedding orientation of the unsteady hairpin vortices becomes asymmetric in $370 \leq Re \leq 460$. The particular flow regime makes the problem challenging and is a good test case to replicate complexities in flow phenomenon where Re can change. In the present case, we are interested in learning the strength and shedding of 3D flow patterns from unsteady planar-symmetric to asymmetric flows for $280 \leq Re \leq 460$.

The point cloud field dataset is processed by interpolating and projecting in the same uniform DL space Ω^{DL} of size

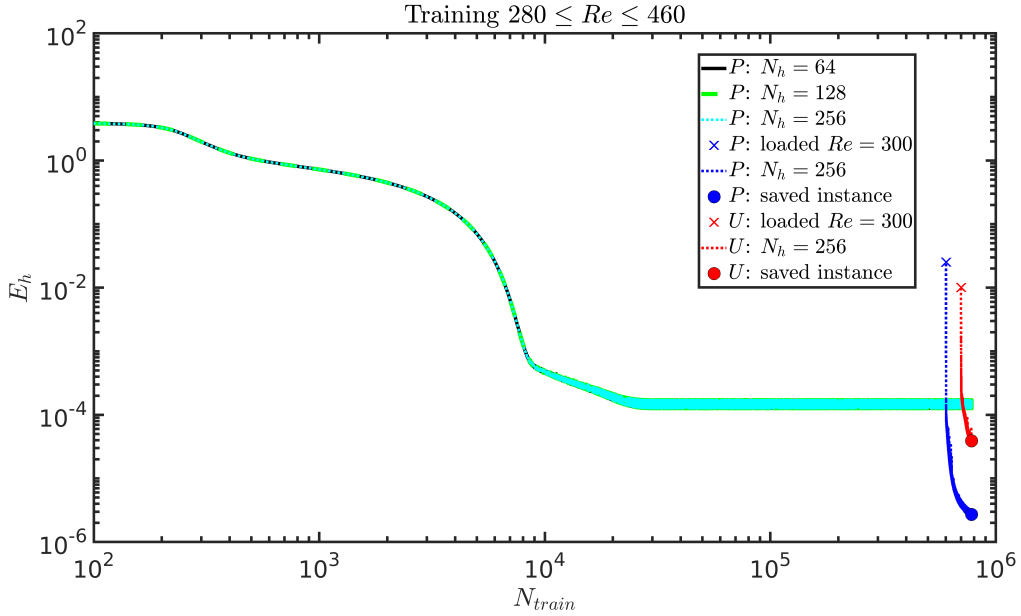


FIG. 14: The variable flow past a sphere: Evolution of the loss function E_h with training iterations for different evolver cell sizes N_h . P and U denote the 3D CRAN models trained with variable Re -based pressure and x-velocity datasets, respectively. The blue cross and red cross represent the initialization of pressure and x-velocity training from optimized single Re 3D CRAN model from Fig. 9. Blue and red dots depict the new saved instances of the 3D CRAN parameters.

$8D \times 8D \times 8D$ using the snapshot-FTLR. Like the single- Re flow scenario, the coarse-grain interpolation and projection of the unstructured dataset are achieved using the linear method on a voxel grid $(N_x \times N_y \times N_z) = (64 \times 64 \times 64)$. The voxel forces from the 3D DL space are corrected by observing functional corrective mapping Ψ for every Re -based flow information. Fig. 13 depicts the voxel force corrections on the training forces, with respective reconstruction error $\epsilon(\cdot)$ for the drag and lift signals over the sphere. It can be interpreted that the mean and derivative error corrections (via Eq. (15)) over various Re numbers on the same 3D DL grid account for the generality of the snapshot-FTLR data recovery process. Irrespective of the flow patterns, the FTLR method recovers the bulk forces within $\epsilon(C_{x,p}) = 0.003$ for drag and $\epsilon(C_{L,p}) = 0.03$ for lift, without requiring a change in the DL grid or grid resolution. Analogous to a single mesh generation process in CFD applications, the snapshot-FTLR method potentially generates a uniform DL grid for the domain-specific problem. Moreover, the inherent unstructured mesh complexity can be bypassed by focussing on a uniform Eulerian grid and 3D CNN operations.

The full-order training dataset matrix $\mathbf{S}(Re_m) \in \mathbb{R}^{N_x \times N_y \times N_z \times (vn_v)}$ consists of $v = 10$ Re numbers and each Re consisting $n_v = 400$ flow snapshots. The scaled flow trainable input $\mathcal{S}(Re_m) = \{\mathcal{S}_s^{I1} \mathcal{S}_s^{I2} \dots \mathcal{S}_s^{IN_s}\} \in [0, 1]^{N_x \times N_y \times N_z \times N_t \times N_s}$ is generated using the basic principles of normalisation and batch-wise arrangement with $N_s = 160$, $N_t = 25$. Note that $\mathcal{S}_s^{Ij} = [\mathbf{S}_{s,j}^{I1} \mathbf{S}_{s,j}^{I2} \dots \mathbf{S}_{s,j}^{IN_t}]$ is a time series data at a particular Re value. The complete spatio-temporal training dataset for the present case is in the order of 1.04×10^9 . The dataset preparation is detailed in section IV C. To train such a big

spatio-temporal dataset on a deep 3D CRAN architecture, we initialize the network training from saved $Re = 300$ parameters as source domain. This is done to gain the advantage of fine-tuning the 3D CRAN for variable Re flow data from single Re flow parameters and bypassing the expensive hyperparameter search. This is further elaborated in Fig. 14 where the evolution of the hybrid loss function E_h is showcased with the training iterations. Every training iteration consists of a mini-batch of size $n_s = 1$ randomly shuffled from the scaled flow input $\mathcal{S}(Re_m)$ and updating the neural parameters in $\approx 0.15s$.

As shown in Fig. 14, the 3D CRAN architecture with $N_h = 64, 128, 256$ does not optimise with a random parameter search for the pressure dataset even after training for ≈ 64 hours on a single GPU. However, the transfer of learning improves traditional learning by transferring knowledge learned in a single Re flow scenario and improving learning in variable Re flow scenarios. With transfer learning, the 3D CRAN starts to optimize from $N_{train} = 10000$ iterations. We save the new 3D CRAN model parameters after $N_{train} = 80000$ for the pressure and x-velocity testing with $E_h = 2.73 \times 10^{-6}$ and 3.90×10^{-5} , respectively. The total offline training time for learning variable Re flow regime took around 3 hours of single GPU training by leveraging single Re flow domain knowledge.

For the data-driven predictions of the pressure and x-velocity, the trained 3D CRAN models with $N_h = 256$ are utilized. We keep the multi-step predictive cycle length of $p = 25$. The predicted and true values of the pressure field at the test time $372.5 tU_\infty/D$ (80th step) are compared in Fig. 15 where the contour plots for $Z/D = 10$ plane are shown. From

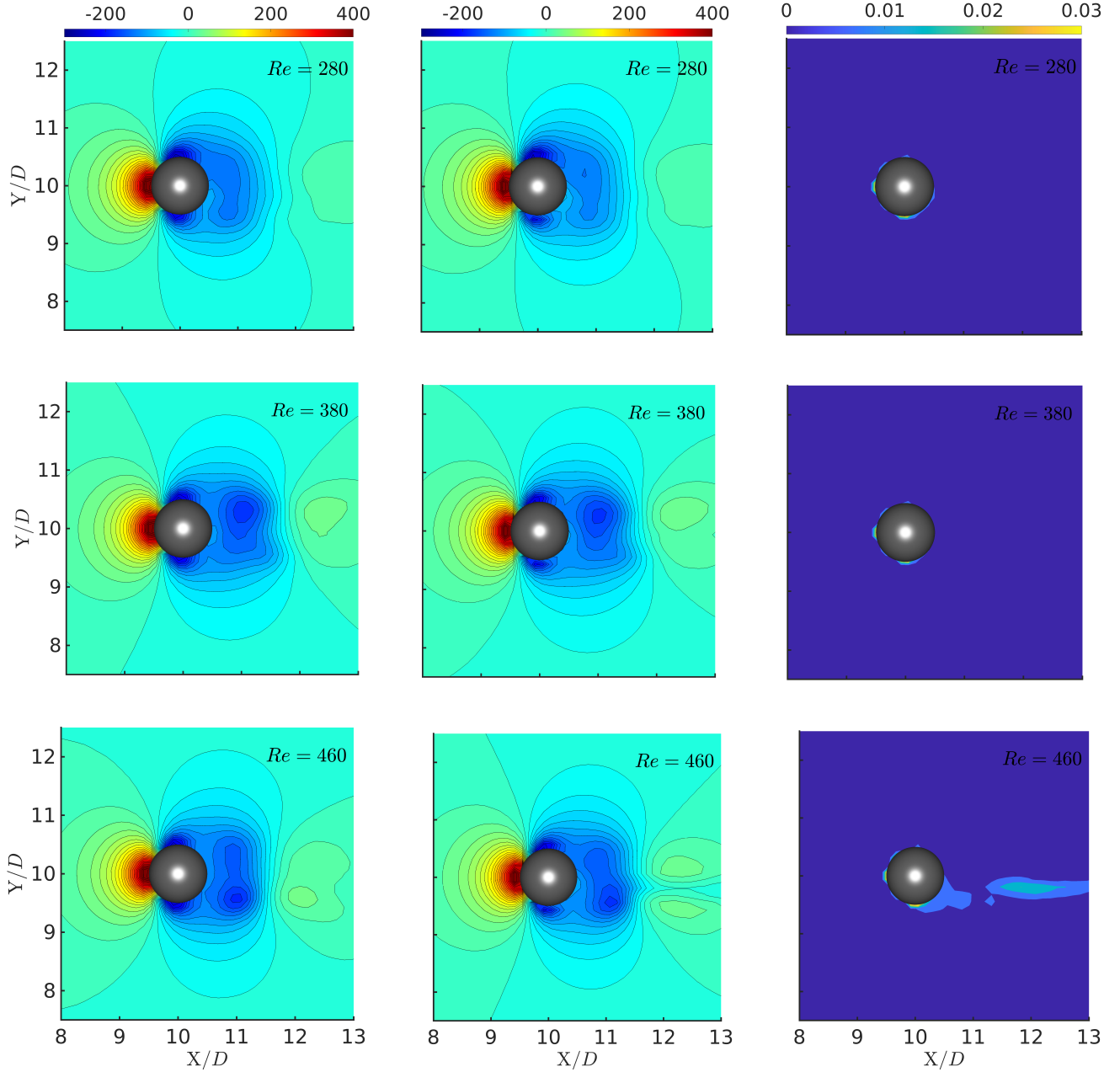


FIG. 15: The variable flow past a sphere: Predicted and true pressure field comparison with normalized reconstruction error E^i at $tU_\infty/D = 372.5$ sliced in $Z/D = 10$ plane. Left, middle and right contour plots depict the prediction, true and errors, respectively.

the reconstruction and inference, it is interesting to observe that the network differentiates and infers in time a specific Re -based field that it is instantiated with. The reconstruction error E^i is calculated by taking the absolute value of the difference between the true and predicted fields and then normalizing it with the truth's L_2 norm for the 3D DL space. The errors are in the order of 10^{-2} near the interface and 10^{-4} elsewhere and are found to increase slightly in the nonlinear wake as the flow becomes asymmetric from $Re \geq 360$. These predictions imply that the network accurately learns the low-dimensional patterns for the variable Re -based flow with limited and unla-

belled information.

Similarly, the profiles of the streamwise velocity from the predicted fields and ground truth are compared in Fig. 16 at test time step $372.5 tU_\infty/D$ in $Z/D = 10$ plane. Closed-loop predictions at all Re are in good agreement with the ground truth velocity in terms of the peak, width, and shape of the streamwise velocity profiles. Velocity profiles at $Y/D = 9.0, 9.5$ show no identifiable differences between the ground truth and 3D CRAN predictions at all Reynolds numbers. This is because flow at $Y/D = 9.0, 9.5$ is almost laminar layer flow, the characteristics of which are relatively easily trained by the

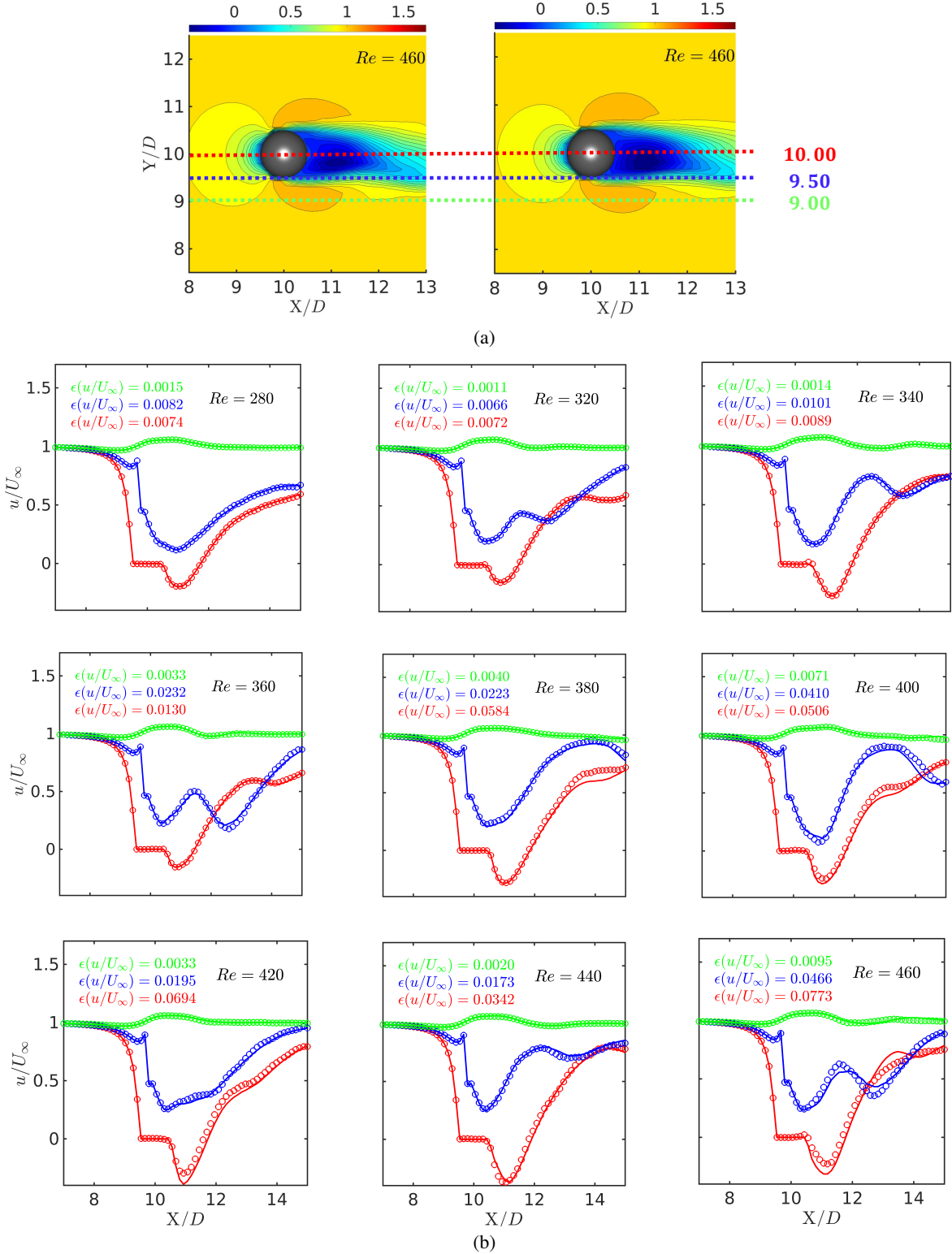


FIG. 16: The variable flow past a sphere: (a) Predicted (left) and true (right) x-velocity field comparison. (b) Comparison of the streamwise velocity profiles of the 3D CRAN prediction and ground truth at three locations $Y/D = 9.0, 9.5, 10$ for all Reynolds numbers. Results are plotted at test time $tU_\infty/D = 372.5$ sliced in $Z/D = 10$ plane. Circles indicate the 3D CRAN predictions, and solid lines represent the ground truth.

network. Minor differences in the velocity deficit are observed for $Y/D = 10.0$ in the nonlinear wake region for $Re \geq 380$ where the 3D CRAN does not accurately capture small-scale oscillatory motions.

Based on the predicted pressure flow fields and the snapshot-FTLR force integration, we discuss the comparison of the mean drag and lift forces from the 3D CRAN prediction and ground truth. Fig. 17 shows the performance of the CRAN-based force predictions when fed with different 3D flow snapshots for Reynolds number $Re \subset Re_m$. To compare the accuracy of the force predictions, we report the R^2 error between the true C_i and predicted \hat{C}_i mean force coefficients calculated using

$$R^2 = 1 - \frac{\sum (\hat{C}_i - \bar{C})^2}{\sum (C_i - \bar{C})^2}. \quad (25)$$

Here, C_i can be the mean drag or lift for a particular Reynolds number. The R^2 errors for the mean drag and lift fit for different Reynolds numbers are 98.58% and 76.43%, respectively, which demonstrates the high efficiency of the CRAN-based prediction process. We find that the predictions perform the best when the field values correspond to $Re \leq 380$, which characterizes a 3D symmetric shedding of the unsteady vortex patterns. Furthermore, when $Re \geq 440$, all the predictions are accurate within a 5% error margin of the FOM results. The performance of the 3D CRAN-based deep learning becomes slightly deficit over the 3D transitional flow regime consisting of $Re = 400, 420$. Interestingly, the maximum prediction errors correspond to this complicated flow from symmetric to asymmetric unsteady patterns. The data of a similar problem may enhance the accuracy of predictions in this transitional flow regime. The most significant result is that the 3D CRAN has accurately captured the maximum and minimum mean drag and lift coefficients for the chosen flow regime $280 \leq Re \leq 460$ in a dearth of training data and on limited training time. Accurate force predictions correspond to a proper field inference from the 3D CRAN framework.

Finally, in Table IV, we provide an estimate of the computational costs for the 3D CRAN together with the full-order simulations for flow past a sphere with variable Reynolds number. We recall that the DL-ROM solution offers remarkable speed-ups in online predictions and offline training in this case. Compared to a 32 CPU parallel FOM solver, a single 3D CRAN framework learns the variable Re flow regime 20 times faster via the transfer learning process. At the same time, the online predictions achieved are 1800 times faster than the parallel FOM solver.

VI. CONCLUSIONS

We have presented a deep learning framework for the reduced-order modeling of three-dimensional unsteady flow, emphasizing variable Re -based flows. The proposed 3D DL-ROM framework relies on the convolutional auto-encoder with recurrent neural networks for data-driven predictions. While the 3D CNNs provide accurate extraction of the

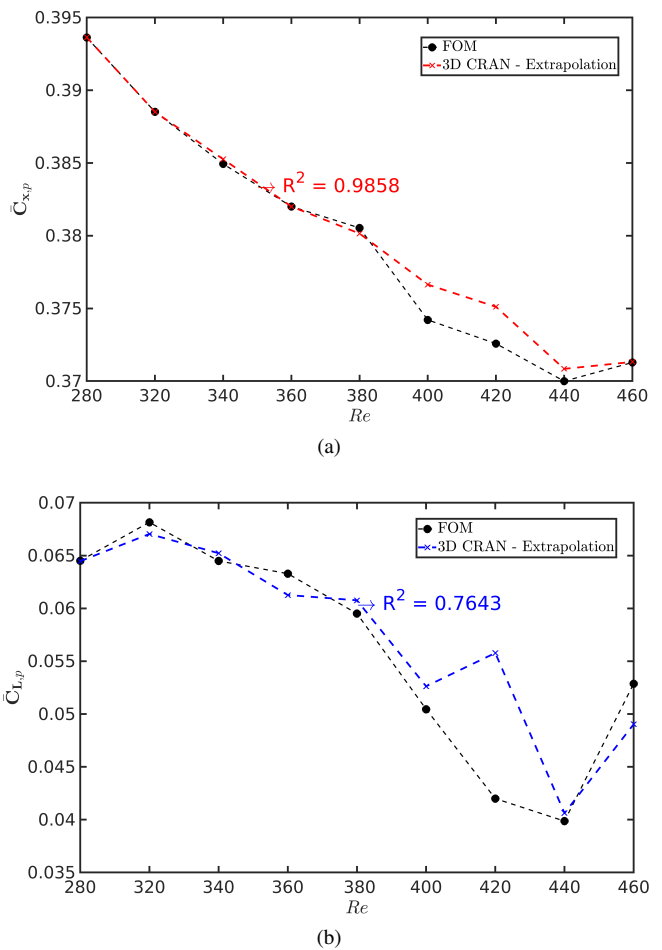


FIG. 17: The variable flow past a sphere: 3D CRAN and FOM comparison of (a) mean drag and (b) mean lift variation over the sphere for different Reynolds numbers.

TABLE IV: Summary of the offline and online times for 3D CRAN vs. 3D FOM simulations for variable Re -based flow.

	FOM-HPC	3D CRAN-PC
Processor number	32 CPUs	1 GPU
Offline time*	≈ 50 h	≈ 2.5 h
Online time**	≈ 10 h	≈ 20 s
Offline speed-up	1	20
Online speed-up	1	1800

* Elapsed time 4000 training steps for 10 Re .

** Elapsed time 1000 test steps for 10 Re .

low-dimensional features from full-order flow snapshots, the LSTM-RNN enables the propagation of the features in time. We have successfully demonstrated the inference capability of the proposed 3D CRAN framework by predicting the time series of the unsteady flow fields of three-dimensional flow past a sphere. Using coarse-grained learning of Re -dependent unsteady flows, a low-dimensional inference of the flow fields with interface load recovery has been discussed.

We have first analyzed an iterative low interface resolu-

tion voxel grid search for the 3D CNNs that preserves the full-order pressure stresses on the fluid-structure interface via snapshot-FTLR. We have shown that this snapshot-FTLR method selects a coarse-grain grid for the CRAN architecture by bringing field uniformity and recovering 3D interface information. This reduces the point cloud complexity and the number of nodes in DL space by 3 times compared to CFD space. An end-to-end 3D CRAN is shown to predict the flow dynamics with accurate estimates of flow prediction at a single Reynolds number. By analyzing an external flow problem past a sphere, we have shown that the 3D CRAN infers and reconstructs the flow fields remarkably for $Re = 300$. The 3D CRAN extrapolates the field from one input data but requires an expensive offline training cost and hyperparameter search. The hyperparameter search has been found to be sensitive to the size of the low-dimensional state of the autoencoder and a detailed study has been performed to tune the network.

For the first time, we have demonstrated the learning and inference capabilities of the 3D CRAN on a complicated symmetry-breaking flow regime ($280 \leq Re \leq 460$) for the flow past a sphere. By leveraging the trained parameters for a single Re , we have shown that 3D CRAN can be trained for a variable Re flow regime on a limited data and training time. Using the process of transfer learning, we achieve the offline training speed-up by nearly 20 times compared to the parallel full-order solver. We find that the predictions perform the best when the field values correspond to $Re \leq 380$, which characterizes a 3D symmetric shedding of the unsteady vortex patterns. Although the network performs reasonably well for asymmetric flows, the maximum prediction errors correspond to the transitional flow regime from symmetric to asymmetric vortex shedding. The 3D CRAN offers nearly three order times faster predictions of 3D flow fields with variable Reynolds numbers using a fraction of training time. It is worth extending the capability of our proposed CRAN framework by incorporating physics-based embedding functions into the autoencoder and considering spatial transformer networks²⁴ to account for globally invariant features.

ACKNOWLEDGEMENTS

The authors would like to acknowledge the Natural Sciences and Engineering Research Council of Canada (NSERC) for the funding. This research was enabled in part through the computational resources and services provided by Compute Canada and the Advanced Research Computing facility at the University of British Columbia.

DATA AVAILABILITY

The data that support the findings of this study are available on request from the authors.

CONFLICT OF INTEREST

The authors declare that they have no conflict of interest.

REFERENCES

- ¹Scipy reference guide, release 1.4.1. <https://docs.scipy.org/doc/scipy-1.4.1/scipy-ref-1.4.1.pdf>, 2019.
- ²S. S. An, T. Kim, and D. L. James. Optimizing cubature for efficient integration of subspace deformations. *ACM Transactions on Graphics*, 165, 2008.
- ³P. Baldi and K. Hornik. Neural networks and principal component analysis: Learning from examples without local minima. *Neural networks*, 2(1):53–58, 1989.
- ⁴S. Bhatnagar, Y. Afshar, S. Pan, K. Duraisamy, and S. Kaushik. Prediction of aerodynamic flow fields using convolutional neural networks. *Computational Mechanics*, pages 1–21, 2019.
- ⁵M. M. Bronstein, J. Bruna, T. Cohen, and P. Veličković. Geometric deep learning: Grids, groups, graphs, geodesics, and gauges. *arXiv preprint arXiv:2104.13478*, 2021.
- ⁶Molly E Brown, David J Lary, Anton Vrieling, Demetris Stathakis, and Hamse Mussa. Neural networks as a tool for constructing continuous ndvi time series from avhrr and modis. *International Journal of Remote Sensing*, 29(24):7141–7158, 2008.
- ⁷S. R. Bukka, R. Gupta, A. R. Magee, and R. K. Jaiman. Assessment of unsteady flow predictions using hybrid deep learning based reduced-order models. *Physics of Fluids*, 33(1):013601, 2021.
- ⁸S. R. Bukka, A. R. Magee, and R. K. Jaiman. Deep convolutional recurrent autoencoders for flow field prediction. In *International Conference on Offshore Mechanics and Arctic Engineering*, volume 84409, page V008T08A005. American Society of Mechanical Engineers, 2020.
- ⁹SANDEEP REDDY BUKKA. *Data-driven computing for the stability analysis and prediction of fluid-structure interaction*. PhD thesis, 2019.
- ¹⁰S. Chaturantabut and D. C. Sorensen. Discrete empirical interpolation for nonlinear model reduction. *SIAM Journal on Scientific Computing*, 32:2737–2764, 2010.
- ¹¹Hu Chen, Yi Zhang, Mannudeep K Kalra, Feng Lin, Yang Chen, Peixi Liao, Jiliu Zhou, and Ge Wang. Low-dose ct with a residual encoder-decoder convolutional neural network. *IEEE transactions on medical imaging*, 36(12):2524–2535, 2017.
- ¹²T. Chen and H. Chen. Universal approximation to nonlinear operators by neural networks with arbitrary activation functions and its application to dynamical systems. *IEEE Transactions on Neural Networks*, 6(4):911–917, 1995.
- ¹³G. Cybenko. Approximation by superpositions of a sigmoidal function. *Mathematics of Control, Signals, and Systems*, 2(4):303–314, 1989.
- ¹⁴G. Dong, G. Liao, H. Liu, and G. Kuang. A review of the autoencoder and its variants: A comparative perspective from target recognition in synthetic-aperture radar images. *IEEE Geoscience and Remote Sensing Magazine*, 6(3):44–68, 2018.
- ¹⁵M. Eichinger, A. Heinlein, and A. Klawonn. Stationary flow predictions using convolutional neural networks. In *Numerical Mathematics and Advanced Applications ENUMATH 2019*, pages 541–549. Springer, 2021.
- ¹⁶N. B. Erichson, M. Muehlebach, and M. W. Mahoney. Physics-informed autoencoders for lyapunov-stable fluid flow prediction. *arXiv preprint arXiv:1905.10866*, 2019.
- ¹⁷S. Fresca and A. Manzoni. Real-time simulation of parameter-dependent fluid flows through deep learning-based reduced order models. *arXiv preprint arXiv:2106.05722*, 2021.
- ¹⁸X. Guo, W. Li, and F. Iorio. Convolutional neural networks for steady flow approximation. In *Proceedings of the 22nd ACM SIGKDD international conference on knowledge discovery and data mining*, pages 481–490, 2016.
- ¹⁹R. Gupta and R. Jaiman. A hybrid partitioned deep learning methodology for moving interface and fluid–structure interaction. *Computers & Fluids*, page 105239, 2021.

- ²⁰P. S. Gurugubelli and R. K. Jaiman. Self-induced flapping dynamics of a flexible inverted foil in a uniform flow. *Journal of Fluid Mechanics*, 781:657–694, 2015.
- ²¹Yoo-Geun Ham, Jeong-Hwan Kim, and Jing-Jia Luo. Deep learning for multi-year ENSO forecasts. *Nature*, 573(7775):568–572, 2019.
- ²²R. Han, Y. Wang, Y. Zhang, and G. Chen. A novel spatial-temporal prediction method for unsteady wake flows based on hybrid deep neural network. *Physics of Fluids*, 31(12):127101, 2019.
- ²³K. Hornik, M. Stinchcombe, and H. White. Universal approximation of an unknown mapping and its derivatives using multilayer feedforward networks. *Neural networks*, 3(5):551–560, 1990.
- ²⁴S. Jaderberg, M. Simonyan, A. Zisserman, and K. Kavukcuoglu. Spatial transformer networks. In *Advances in Neural Information Processing Systems 28 (NIPS 2015)*, 2015.
- ²⁵R. Jaiman, P. Geubelle, E. Loth, and X. Jiao. Transient fluid–structure interaction with non-matching spatial and temporal discretizations. *Computers & Fluids*, 50(1):120–135, 2011.
- ²⁶R. K. Jaiman, M. Z. Guan, and T. P. Miyanawala. Partitioned iterative and dynamic subgrid-scale methods for freely vibrating square-section structures at subcritical Reynolds number. *Computers & Fluids*, 133:68–89, 2016.
- ²⁷R. K. Jaiman and V. Joshi. *Computational Mechanics of Fluid-Structure Interaction*. Springer, 2022.
- ²⁸X. Jin, P. Cheng, W. Chen, and H. Li. Prediction model of velocity field around circular cylinder over various Reynolds numbers by fusion convolutional neural networks based on pressure on the cylinder. *Physics of Fluids*, 30(4):047105, 2018.
- ²⁹TA Johnson and VC Patel. Flow past a sphere up to a Reynolds number of 300. *Journal of Fluid Mechanics*, 378:19–70, 1999.
- ³⁰V. Joshi and R. K. Jaiman. A hybrid variational Allen-Cahn/ALE scheme for the coupled analysis of two-phase fluid-structure interaction. *International Journal for Numerical Methods in Engineering*, 117(4):405–429, 2019.
- ³¹Anuj Karpatne, William Watkins, Jordan Read, and Vipin Kumar. Physics-guided neural networks (pgnn): An application in lake temperature modeling. *arXiv preprint arXiv:1710.11431*, 2017.
- ³²S. R. Kashyap and R. K. Jaiman. A robust and accurate finite element framework for cavitating flows with fluid-structure interaction. *Computers & Mathematics with Applications*, 103:19–39, 2021.
- ³³D. P. Kingma and J. Ba. Adam: A method for stochastic optimization. *arXiv preprint arXiv:1412.6980*, 2014.
- ³⁴S. Lee and D. You. Data-driven prediction of unsteady flow over a circular cylinder using deep learning. *Journal of Fluid Mechanics*, 879:217–254, 2019.
- ³⁵Y. Lee, H. Yang, and Z. Yin. Piv-dcnn: cascaded deep convolutional neural networks for particle image velocimetry. *Experiments in Fluids*, 58(12):171, 2017.
- ³⁶Sebastian Lunz, Ozan Öktem, and Carola-Bibiane Schönlieb. Adversarial regularizers in inverse problems. In *Advances in Neural Information Processing Systems*, pages 8507–8516, 2018.
- ³⁷M. Ma, C. Sun, and X. Chen. Deep coupling autoencoder for fault diagnosis with multimodal sensory data: an efficient deep learning. *IEEE Transactions on Industrial Informatics*, 14(3):1137–1145, 2018.
- ³⁸T. P. Miyanawala and R. K. Jaiman. An efficient deep learning technique for the Navier-Stokes equations: Application to unsteady wake flow dynamics. *arXiv preprint arXiv:1710.09099*, 2017.
- ³⁹T. P. Miyanawala and R. K. Jaiman. Decomposition of wake dynamics in fluid–structure interaction via low-dimensional models. *Journal of Fluid Mechanics*, 867:723–764, 2019.
- ⁴⁰T. P. Miyanawala and R. K. Jaiman. A hybrid data-driven deep learning technique for fluid-structure interaction. In *International Conference on Offshore Mechanics and Arctic Engineering*, volume 58776, page V002T08A004. American Society of Mechanical Engineers, 2019.
- ⁴¹T. Murata, K. Fukami, and K. Fukagata. Nonlinear mode decomposition with convolutional neural networks for fluid dynamics. *Journal of Fluid Mechanics*, 882, 2020.
- ⁴²F. Ogoke, K. Meidani, A. Hashemi, and A. B. Farimani. Graph convolutional neural networks for body force prediction. *arXiv preprint arXiv:2012.02232*, 2020.
- ⁴³Eric J Parish and Karthik Duraisamy. A paradigm for data-driven predictive modeling using field inversion and machine learning. *Journal of Computational Physics*, 305:758–774, 2016.
- ⁴⁴D. Park, Y. Hoshi, and C. C. Kemp. A multimodal anomaly detector for robot-assisted feeding using an LSTM-based variational autoencoder. *IEEE Robotics and Automation Letters*, 3(3):1544–1551, 2018.
- ⁴⁵S. Peitz and S. Klus. Koopman operator-based model reduction for switched-system control of PDEs. *Automatica*, 106:184–191, 2019.
- ⁴⁶T. Pfaff, M. Fortunato, A. Sanchez-Gonzalez, and P. W. Battaglia. Learning mesh-based simulation with graph networks. *arXiv preprint arXiv:2010.03409*, 2020.
- ⁴⁷E. Plaut. From principal subspaces to principal components with linear autoencoders. *arXiv preprint arXiv:1804.10253*, 2018.
- ⁴⁸J. Rabault, J. Kolaas, and A. Jensen. Performing particle image velocimetry using artificial neural networks: a proof-of-concept. *Measurement Science and Technology*, 28(12):125301, 2017.
- ⁴⁹M. Raissi, P. Perdikaris, and G. E. Karniadakis. Physics-informed neural networks: A deep learning framework for solving forward and inverse problems involving nonlinear partial differential equations. *Journal of Computational Physics*, 378:686–707, 2019.
- ⁵⁰Omer San and Romit Maulik. Machine learning closures for model order reduction of thermal fluids. *Applied Mathematical Modelling*, 60:681–710, 2018.
- ⁵¹A. Sanchez-Gonzalez, J. Godwin, T. Pfaff, R. Ying, J. Leskovec, and P. Battaglia. Learning to simulate complex physics with graph networks. In *International Conference on Machine Learning*, pages 8459–8468. PMLR, 2020.
- ⁵²P. J. Schmid. Dynamic mode decomposition of numerical and experimental data. *Journal of fluid mechanics*, 656:5–28, 2010.
- ⁵³J. R. Singler. Balanced POD for model reduction of linear PDE systems: convergence theory. *Numerische Mathematik*, 121(1):127–164, 2012.
- ⁵⁴L. Sirovich. Turbulence and the dynamics of coherent structures. i. coherent structures. *Quarterly of applied mathematics*, 45(3):561–571, 1987.
- ⁵⁵K. Taira, S. L. Brunton, S. Dawson, C. W. Rowley, T. Colonius, B. J. McKeon, O. T. Schmidt, S. Gordeyev, V. Theofilis, and L. S. Ukeiley. Modal analysis of fluid flows: An overview. *arXiv preprint arXiv:1702.01453*, 2017.
- ⁵⁶J. Wang, J. Wu, and H. Xiao. Physics-informed machine learning approach for reconstructing Reynolds stress modeling discrepancies based on DNS data. *Physical Review Fluids*, 2(3):034603, 2017.
- ⁵⁷J. Yu, C. Hong, Y. Rui, and D. Tao. Multitask autoencoder model for recovering human poses. *IEEE Transactions on Industrial Electronics*, 65(6):5060–5068, 2017.
- ⁵⁸Y. Zhu, N. Zabarbas, P. Koutsourelakis, and P. Perdikaris. Physics-constrained deep learning for high-dimensional surrogate modeling and uncertainty quantification without labeled data. *Journal of Computational Physics*, 394:56–81, 2019.